AFOSR-TR. 85-1102

AD-A162 354

ARPA Order:	4983
Program Code:	5D60
Name of Grantee:	Regents of the University of California University of California, San Diego Scripps Institution of Oceanography La Jolla, California 92093
Effective Date of Grant:	1 January 1985
Grant Expiration Date:	31 December 1985
Amount of Grant Dollars:	$171,012
Grant Number:	AFOSR-84-0043
Principal Investigator:	John A. Orcutt (619) 452-2887
Program Manager:	Dr. Henry Radoski (202) 767-4904
Short Title of Work:	Analysis of MSS and OBS Data Collected During the NGENDEI Seismic Experiment.

DTIC
ELECTE
DEC 0 9 1985
S D
D

DTIC FILE COPY

The views and conclusions contained in this document are those of the authors
and should not be interpreted as necessarily representing the official policies,
either expressed or implied, of the Defense Advanced Research Projects Agency or
the U.S. Government.

85 12 -6 074

REPORT DOCUMENTATION PAGE

1a. REPORT SECURITY CLASSIFICATION		1b. RESTRICTIVE MARKINGS		
2a. SECURITY CLASSIFICATION AUTHORITY		3. DISTRIBUTION/AVAILABILITY OF REPORT		
2b. DECLASSIFICATION/DOWNGRADING SCHEDULE		Approved for public release; distribution unlimited.		
4. PERFORMING ORGANIZATION REPORT NUMBER(S)		5. MONITORING ORGANIZATION REPORT NUMBER(S) AFOSR-TR- 85-1102		
6a. NAME OF PERFORMING ORGANIZATION University of California Scripps Inst. of Oceanography	6b. OFFICE SYMBOL (If applicable)	7a. NAME OF MONITORING ORGANIZATION AFOSR		
6c. ADDRESS (City, State and ZIP Code) Scripps Institution of Oceanography La Jolla California 92093		7b. ADDRESS (City, State and ZIP Code) AFOSR Bldg. 410 Bolling Air Force Base, D.C. 20332		
8a. NAME OF FUNDING/SPONSORING ORGANIZATION ARPA	8b. OFFICE SYMBOL (If applicable)	9. PROCUREMENT INSTRUMENT IDENTIFICATION NUMBER AFOSR-84-0043		

8c. ADDRESS (City, State and ZIP Code) ARPA 1400 Wilson Blvd. Arlington. VA 22209	10. SOURCE OF FUNDING NOS.			
	PROGRAM ELEMENT NO. 61101E	PROJECT NO. AO 4397	TASK NO. 05	WORK UNIT NO.

11. TITLE *(Include Security Classification)*
Analysis of MSS and OBS Data Collected During the NGENDEI Seismic Experiment

12. PERSONAL AUTHOR(S)
John A. Orcutt

13a. TYPE OF REPORT Semi-Annual	13b. TIME COVERED FROM 1 Jan 85 TO 30 Aug 85	14. DATE OF REPORT (Yr., Mo., Day) August 1985	15. PAGE COUNT 64

16. SUPPLEMENTARY NOTATION

17.	COSATI CODES		18. SUBJECT TERMS *(Continue on reverse if necessary and identify by block number)*
FIELD	GROUP	SUB. GR.	

19. ABSTRACT *(Continue on reverse if necessary and identify by block number)*

The results of the first year's data analysis employing data collected during the NGENDEI seismic experiment in the southwest Pacific are presented. This experiment tested the DARPA Marine Seismic System and verified the improved signal-to-noise ratio achieved by burying the instrument within the oceanic crust. Generally, all the goals of the experiment were achieved and a number of very exciting results are reported.

next page

20. DISTRIBUTION/AVAILABILITY OF ABSTRACT	21. ABSTRACT SECURITY CLASSIFICATION
UNCLASSIFIED/UNLIMITED ☑ SAME AS RPT. ☐ DTIC USERS ☐	UNCLASSIFIED
22a. NAME OF RESPONSIBLE INDIVIDUAL Dr Kelley	22b. TELEPHONE NUMBER (Include Area Code) (202) 767-4908	22c. OFFICE SYMBOL NP

DD FORM 1473, 83 APR   EDITION OF 1 JAN 73 IS OBSOLETE.

SUMMARY

This Semi-Annual Technical Report provides an update on progress in the analysis of the seismic data collected during the "NGENDEI" Experiment sponsored by DARPA in early 1983 in the southwest Pacific. The experiment, which took place on the Deep Sea Drilling Project Leg 91, was designed to test the Marine Seismic System (MSS) in a realistic environment near an active trench environment. An earlier test of the system in the northwest Pacific had been unsuccessful because of difficulties in drilling an acceptable borehole in the seafloor. The Scripps' ship, the R/V Melville, was used in addition to the D/V Glomar Challenger for tasks related to site surveying, ocean bottom seismograph (OBS) deployment and refraction shooting. Chief Scientists on the expedition were John Orcutt and Tom Jordan on the Melville and Bill Menard and Jim Natland on the Challenger. The experiment was quite successful and accomplished all major goals. The MSS was recorded aboard the D/V Glomar Challenger for several days of earthquake, refraction and environmental noise experiments. The subsequent deployment of an autonomous recording package on the seafloor was successful, but a leak in one of the spheres housing the batteries resulted in a power loss after approximately two days. The OBS's launched several times during the course of the experiment operated correctly in all instances including the 45 day teleseismic recording phase at the end. The MSS recording package as well as the six OBS's were recovered at the end of the experiment by the R/V Melville. The MSS was left in the borehole and the co-axial cable was terminated in a dummy load. The mooring system used for recovery was redeployed in the event a future experiment became necessary or desireable.

The two chapters of this report are composed of papers which have either been accepted for publication (Chapter 1) or submitted for review (Chapter 2). Papers prepared under the terms of this grant, and which are available in this or the previous Annual Technical Report, include:

1. Shearer, P. and J. Orcutt, 1985. Anisotropy in the oceanic lithosphere - Theory and observations from the NGENDEI seismic refraction experiment in the southwest Pacific, Geophys. J. R. astr. Soc., 80, 493-526.

2. Sereno, T.J. and J.A. Orcutt, 1985. Synthetic seismogram modeling of the oceanic P_n phase, Nature, 316, 246-248.

3. Sereno, T.J. and J.A. Orcutt, 1985. The synthesis of realistic oceanic P_n wavetrains, Jour. Geophys. Res., in press.

4. Adair, R.G., J.A. Orcutt and T.H. Jordan, 1985. Ocean-bottom infrasonic, and ocean-bottom and sub-bottom seismic noise observations in the deep sea: Results from the NGENDEI Experiment, Jour. Acoust. Soc. Am., submitted.

5. Sereno, T.J. and J.A. Orcutt, 1985. The propagation of P_n, Proceedings of the La Spezia Symposium on Seismo-Acoustics, Plenum Press, in press.

6. Kim, I.I., D.K. Smith, H.W. Menard, J.A. Orcutt and T.H. Jordan, 1985. Seismic reflection site survey: Correlation with physical properties, Leg 91, Deep Sea Drilling Project, Initial Reports of the Deep Sea Drilling Project, submitted.

7. Adair, R.G., M. Harris, J.A. Orcutt and T.H. Jordan, 1985. Description and performance of the Marine Seismic System during the NGENDEI Experiment, Initial Reports of the Deep Sea Drilling Project, submitted.

8. Orcutt, J.A., R.D. Moore and T.H. Jordan, 1985. Description and performance of the Scripps ocean bottom seismographs during the NGENDEI Experiment, Initial Reports of the Deep Sea Drilling Project, submitted.

9. Adair, R.G., J.A. Orcutt and T.H. Jordan, 1985. Preliminary analysis of ocean bottom and sub-bottom ambient microseismic noise during the NGENDEI Experiment, Initial Reports of the Deep Sea Drilling Project, submitted.

10. Shearer, P.M., R.G. Adair, J.A. Orcutt and T.H. Jordan, 1985. Simultaneous borehole and ocean bottom seismometer recordings of earthquakes and explosions - Results from the 1983 NGENDEI Experiment at DSDP Hole 595B, Initial Reports of the Deep Sea Drilling Project, submitted.

11. Shearer, P.M., J.A. Orcutt, T.H. Jordan, R.B. Whitmarsh, I.I. Kim, R.G. Adair, and M.S. Burnett, 1985. The NGENDEI seismic refraction experiment at DSDP Hole 595B - Ocean bottom seismometer data and evidence for upper mantle anisotropy, Initial Reports of the Deep Sea Drilling Project, submitted.

12. Whitmarsh, R.B., J.A. Orcutt, T.H. Jordan, R.G. Adair and P.M. Shearer, 1985. Velocity bounds on the seismic structure of late Jurassic (157 Ma old) crust and upper mantle in the southwest Pacific basin from downhole observations at Deep Sea Drilling Project Hole 595B, Initial Reports of the Deep Sea Drilling Project, in press.

Chapter 1 of this report discusses a propagation model for the oceanic regional phase P_n in which the onset consists of a refraction from the relatively high-Q oceanic lithosphere while the extensive coda is a result of near-receiver sediment and water reverberation. This model contrasts sharply with proposed scattering mechanisms for generating the observed coda and receives strong support from the numerical modeling and the high quality oceanic earthquake data collected in this program. In addition to generating realistic coda associated with P_n and S_n wavetrains, the model has successfully predicted the absolute amplitudes of observations collected during NGENDEI so that the model can be confidently used for predictive purposes. The reverberations induced in the sediment and ocean column give rise to "eigenfrequencies" associated with leaky organ pipe modes in the water column (acoustic only) and sediment section (elastic waves). These eigenfrequencies are readily isolated in both the synthetics and data and are consistent with physical properties measurements conducted at the drill site. The horizontal component data and synthetic spectra are dominated by the fundamental shear mode. This mode gives rise to the characteristic monochromatic reverberations typical of marine horizontal components. We have observed that the P_n phases recorded during the experiment are quite coherent when the data are high passed above the fundamental shear eigenfrequency for sediment reverberations. This is a sensible behavior given that the greatest source of local heterogeneity on the seafloor is the spatial variation of sediment thickness. Finally, in this chapter, we note that the observed decrease in P_n group velocity at a range of about 30° results from the introduction of a mid-point reflection from the free surface of the lithosphere refracted phase and that the required thickness of the lithosphere is quite large - 200 km.

The computations which support the work on the regional phases are quite intensive numerically and require large amounts of computer time. We have increased the shear Q used in the calculations described in Chapter 1 from 225 to 1000 and have repeated the synthesis of the complete seismograms. The S_n phase is now much more realistic than that presented in Chapter 1. Computations in the future will be run with the goal of narrowing the current loose constraints on the lithosphere attenuation properties. The current computation is being extended to higher frequencies to permit a more thorough study of the Q. The algorithm we use for these complete calculations is being modified to run on a CRAY 1 at the CRAY headquarters in Chippewa Falls and will be used extensively on the CRAY XMP/48 currently being installed at the NSF-sponsored San Diego Supercomputer Center.

Chapter 2 presents simultaneous measurements of ocean bottom infrasonic and ocean bottom and sub-bottom seismic noise in the frequency band 0.1-20 Hz. In the band 0.1-1 Hz, noise propagation as seismic modes trapped near the seafloor is supported by observed spectral coherences, cross-phases and ratios between ocean bottom pressure and vertical ground motion, and by the relatively lower noise levels in the borehole. Noise variations in this band are clearly correlated with changes in local wind direction and speed, presumably through ocean bottom pressure fluctuations caused by nonlinear wind wave-wind wave and wind wave-

swell interaction. The growth of spectral peaks and generally increased levels over the microseism band in both seismic and acoustic measurements followed sharp changes in wind direction. Activity in the microseism band abated as the wind persisted or died away. Amplitude and phase relationships between pressure and vertical seismic motion at the microseism periods imply that a portion of the noise propagated as trapped modes of the ocean-seafloor system. The appearance of peaks at periods corresponding to acoustic reverberations in the water-sediment column suggests that some of the ambient noise may be due to (leaky) organ pipe modes. These observations constitute the first comparison of simultaneous ocean bottom and sub-bottom seismic noise and ocean bottom noise over the microseism band in the deep ocean. Recent quantitative experiments with the same algorithm used in the wave propagation studies discussed above have resulted in a successful replication of observed noise spectral shapes and amplitudes.

I have proposed to continue aspects of this research upon expiration of this grant in January, 1986. In particular, I have suggested comparing noise levels observed on the seafloor with those typically encountered on islands. Because of breaking waves, islands are frequently quite noisy. It is likely that, for much of the discrimination band, adjacent seafloor noise levels are much lower. If this proved to be the case, the installation of stations 50-100 km off islands with co-axial or fiber optic cabling could enhance current detection and discrimination capabilities.

The analyses conducted with oceanic regional data under this grant have concentrated on the results of the NGENDEI experiment. I have proposed to check additional data, in particular that available from the Wake Island Array, for the same systematics so clearly observed in the NGENDEI data. This study would serve as a rigorous test of the propagation models for oceanic regional phases which we have developed during the past year.

Finally, I have proposed to apply many of the things we've learned about regional wave propagation to the study of continental phases (L_g, P_g, R_g, P_n, S_n) as recorded by the new, digital NORESS array. These phases are, of course, of great interest at high frequencies in nuclear test discrimination and detection. The NORESS array is ideally suited to frequency and wavenumber analyses of such high wavenumber phenomena and comparisons with computed responses. The oceanic data are intrinsically limited to studies in the temporal and frequency domains since the small number and large inter-instrument distances preclude wavenumber estimates. I feel the extension of these quantitative studies to the NORESS data would be immensely rewarding and is a program I consider to be quite important.

CHAPTER 1

THE PROPAGATION OF P_a

Thomas Sereno and John Orcutt

Institute of Geophysics and Planetary Physics
Scripps Institution of Oceanography, A-025
La Jolla, California 92093

ABSTRACT

A propagation model for the oceanic P_n phase is presented in which the onset consists of a refraction from the lower oceanic lithosphere while the subsequent coda is a result of near-receiver sediment and water reverberation. The first arrival of the oceanic P_n phase remains entirely within the lithosphere and for epicentral ranges in excess of 25° to 30° contains a free surface reflection, similar to the seismic phase PP. At large epicentral distances, or similarly for deep events, the P_n wavetrain is preceded by a low frequency forerunner which has traversed the low Q asthenosphere. The coda of the P_n phase was analyzed through the computation of synthetic seismograms using wave number integration. Spectral characteristics associated with both sediment and water reverberation are clearly observed in both the synthetics and data collected in the southwest Pacific during the 1983 Ngendei Seismic Experiment.

INTRODUCTION

The oceanic P_n phase is characterized by low spatial attenuation, a high frequency wavetrain of extremely long duration and an onset velocity near 8.0 km/s[1]. Through the computation of synthetic seismograms in a laterally homogeneous, vertically stratified medium we will show that these properties can be achieved in the absence of scattering, low velocity channels or high Q waveguides.

SYNTHETIC SEISMOGRAMS

Wave number integration, in which a quadrature over wave number is performed at fixed frequency points, was used to generate the synthetic seismograms[2]. The time domain response was obtained by applying a Fourier transform to the resulting complex spectrum. The seismograms contain all reverberations, including those off the free surface, as well as all P to S and S to P mode conversions. Attenuation is included by allowing the material velocities to be complex thereby allowing the integration to be performed

along the real wave number axis. The most serious limitations of the method include the restriction to models consisting of a stack of homogeneous layers and the high computational costs involved for models with more than 10 to 15 layers.

As an exploratory model we have adopted that of Gettrust and Frazer[3] which includes a 4 km thick water layer and a 500 m thick sediment layer overlying a vertically inhomogeneous oceanic crust and upper mantle. Compressional and shear wave velocities are monotonically increasing functions of depth. The values of the quality factor, Q, were less than 500 in the crust and upper mantle and 50,000 in the oceanic water column.

Figure 1 is an example of complete synthetic seismograms generated for a sub-Moho thrust fault at an epicentral range of 1000 km. The late arriving energy on the vertical component (figure 1a) with a group velocity of 1.6 km/s is emergent in nature and has a substantial duration characteristic of oceanic abyssal T-phases[4]. Through a comparison of delay time wavefields between Green's functions that contain this late arriving energy and Green's functions that do not, it was observed that the ray parameter range comprising this group corresponds to that of post-critical reflections off the Moho. The synthetic T-phase is thus explained as a reverberation between the free surface and the Moho with a substantial number of water and crustal reverberations acting to extend the wavetrain. The 4.7 km/s arrival on the horizontal component (figure 1b) is grossly identified as the oceanic S_n phase. The first arrivals of this group are horizontally polarized shear waves and are thus absent from the vertical component. Work is continuing in an effort to synthesize more realistic S_n phases.

The synthetic P_n wavetrain has an onset velocity of 8.1 km/s, a duration of over 100 seconds and extends into the onset of S_n. The amplitude of the synthetic P_n wavetrain was within a factor of 2 or 3 of data amplitudes obtained during the 1983 Ngendei Seismic Experiment in the southwest Pacific (23° 49'S, 165° 32'W). An event located near the Tonga Islands by the National Earthquake Information Service (NEIS) with a magnitude of 5.8 and a moment of 2.6 x 10^{24} dyne-cm was recorded by three ocean

bottom seismometers (OBS's) at the Ngendei site. The maximum amplitudes of these recordings ranged between 0.76 and 1.44 volts. Convolution of the synthetic P_n phase with the OBS instrument response and scaling by the NEIS published moment yielded a maximum amplitude of 0.42 volts. Differences of this order can be explained simply in terms of differences in model parameters, fault orientation and focal depth.

REVERBERATIONS

The importance of reverberations within the oceanic water column and sediment layer is most effectively demonstrated in the frequency domain. It is simple to show that the power spectrum of a wavelet reverberating in a single layer has eigenfrequencies given by

$$f_n = (2n+1)\frac{df}{2} \quad n = 0,1,2,... \tag{1}$$

where $df = 1/T$ and T is the time between multiples. In the case of near-vertical incidence T can be approximated by the two-way travel time in the layer and (1) represents the eigenfrequencies for an organ-pipe mode[5]. Arrivals within the P_n wavetrain must penetrate the mantle in order to have group velocities between 6 and 8 km/s and must therefore have phase velocities greater than 8 km/s. A result of this is that the rays are quite steep at the receiver, justifying the use of the two-way travel time in equation (1). The $df/2$ offset of the spectral peaks is due to a π-phase shift between multiples. The width of the spectral peaks at frequencies given by (1) is governed by the impedance contrast at the boundaries of the layer. Thus leaky modes, which suffer a continuous loss of energy along the propagation path due to leakage into the surrounding medium, will attenuate more rapidly than locked modes and will thus have substantially wider spectral peaks. The decay of the reverberation peaks with increasing mode number, n, is a function of Q in the layer.

The computation of the full synthetic seismograms pictured in figure 1 required extremely fine frequency sampling to avoid time series wrap-around. The calculation extended to a Nyquist frequency of only 6.4 Hz which involved obtaining the response at 8193 frequency points. While the wave number integration algorithm is not strictly bandlimited, the costs of extending the calculation to higher frequencies are formidable. Synthetic power spectra do not, however, require this fine frequency sampling and can be computed rather efficiently up to a Nyquist frequency of 64.0 Hz. Thus direct comparison between data collected at the Ngendei site and synthetics is easily achieved in the frequency domain.

The Ngendei site was the location of hole 595B of Deep Sea Drilling Project (DSDP), Leg 91. The depth of the oceanic water column at the site is 5.5 km and, from core sample measurements, the sediment thickness is 70 m with a compressional velocity of 1.6 km/s[6]. For compressional wave sediment reverberation the two-way travel time in the layer is 0.0875 s yielding an eigenfrequency spacing of $df=11\ 43$ Hz. The impedance contrast at the ocean-sediment interface is quite small for compressional waves. Thus the sediment layer acts as an extremely leaky waveguide for compressional wave propagation and the peaks associated with sediment reverberation have a large characteristic width. The reverberations within the water column actually include the sediment layer and take place between the free surface and the base of the sediments. The resulting eigenfrequency spacing for water reverberations is therefore $df=.1375$ Hz. Both interfaces in this case have very strong impedance contrasts and the associated spectral peaks are quite narrow. Thus the power spectrum of a wavelet reverberating in the oceanic water column and sediment layer consists of widely spaced spectral "humps" due to P-wave sediment reverberation superimposed on finely spaced spectral "peaks" due to water reverberation.

Figure 2 is an illustration of this behavior. Figure 2b is a synthetic power spectrum computed using wave number integration in which we have used the sediment and water properties of the Ngendei site. In an effort to reduce computational costs we have

included only phase velocities between 6.9 and 25.0 km/s. Figure 2a depicts the first 3.0 Hz of the spectrum with vertical lines indicating the eigenfrequencies of water reverberation computed using equation (1). Figure 2b contains the full spectrum after correcting for the OBS instrument response and a source spectrum[5] of the form

$$\left| S(f) \right|^2 = S(0)^2 \left[1 + \frac{f}{f_c} \right]^{-4} \tag{2}$$

where f_c is the corner frequency and was given a value of 0.6 Hz. In this case the vertical lines indicate positions of spectral "humps" associated with P-wave sediment reverberation. To verify our interpretation of these features we doubled the layer thicknesses and recomputed the spectra. The effect was to decrease the spacing of the spectral peaks by a factor of 2 thereby validating the interpretation.

Figures 2c and 2d contain power spectra of data collected at the Ngendei site. Figure 2c is the first 3.0 Hz of a hydrophone spectrum illustrating the presence of water reverberations and figure 2d is an OBS vertical component spectrum illustrating the presence of sediment reverberation. These spectral features were quite common in the data and were independent of the source characteristics.

The presence of S-wave sediment reverberation is most easily detected in horizontal component spectra due to the steep incidence of the rays. For shear waves the impedance contrasts at both the ocean-sediment and sediment-crust interfaces are quite large yielding relatively narrow spectral peaks. The low quality factor for shear waves in the sediments, however, results in a rapid decay of the spectral peaks with increasing mode number. Figure 3a depicts the first 3.0 Hz of the synthetic horizontal component power spectrum after including the OBS instrument response and source spectrum given by (2). The shear wave sediment velocity used in the computation of the synthetic spectrum was 116 m/s yielding an eigenfrequency spacing of 0.83 Hz. Figure 3b is the synthetic spectrum without including the instrument response. Figure 3c is the first 3.0 Hz of the power spectrum of horizontal component data taken at the Ngendei site and 3d was obtained

after removing the instrument response. In figures 3a-3d, dashed vertical lines indicate predicted frequencies (equation (1)) of spectral peaks associated with S-wave sediment reverberation. The positions, widths and spectral decay rates of these peaks all agree with pre-dictions for shear wave sediment reverberation. Once again we altered the sediment thickness and recomputed the spectra to verify our interpretation of the peaks in the synthetic spectra.

COHERENCE

Strong coherence of the P_n wavetrain between OBS's separated by large distances is not expected unless the water and sediment properties at the two sites are nearly equal. It was found in the Ngendei data that far greater coherence could be achieved by bandpassing the data between 2.0 and 25.0 Hz prior to comparison. The result of even a small change in either S-wave sediment velocity or sediment thickness would result in a measurable shift in the dominan, frequency of the wavetrain (figure 3). The frequency band between 0.0 and 2.0 Hz is the most sensitive to these changes resulting in a reduction of coherence at these lower frequencies. Figure 4 is a comparison of data collected by two different OBS's separated by a distance of 1.9 km for the same event after bandpassing between 2.0 and 25.0 Hz. The first water reverberation is evident at about 9 seconds and the excellent coherence well into the P_n wavetrain is evidence for reverberation, as opposed to scattering, as the dominant mechanism of P_n coda generation. Work is continuing on the problem of coherence as well as that of polarization within the P_n coda.

PROPAGATION PATH

The observation that the group velocity of P_n is generally higher at epicentral ranges between 12° and 30° than at distances outside this range[7] can be explained by the confinement of P_n to the oceanic lithosphere. At ranges less than 30° the onset of P_n is associated with a normal refracted P-wave remaining in the lithosphere, however at dis-

tances in excess of 30° the first arrival that remains in the lithosphere contains a free surface reflection, similar to the seismic phase PP, thereby decreasing the group velocity. This is demonstrated in figure 5b which displays the group velocity of P_n as a function of epicentral distance for the velocity model shown in figure 5a. In order to achieve a crossover distance of 30°, a lithosphere thickness of nearly 200 km is required. The decrease in group velocity at ranges less than 12° is the result of shallower turning points in the lithosphere. A similar interpretation was presented by Menke and Richards[8] in terms of whispering gallery modes at the Moho.

Figure 5c is a travel time curve illustrating the arrival times of normal refracted P verses P_n for the model in figure 5a. The curves diverge at an approximate range of 25° where the normal refracted arrival is a ray that has crossed the low Q asthenosphere constituting the commonly observed low frequency forerunner of the P_n wavetrain[9]. Figure 6 is an example illustrating the normal refracted P forerunner of oceanic P_n. For deep events the separation of normal refracted P and P_n occurs for smaller ranges as P_n must propagate up and around the corner of the descending slab. During the Ngendei Experiment the deployment of a continuously recording borehole seismometer enabled the recording of strong P_n phases for events with focal depths in excess of 450 km. The suggestion that a descending slab can act as a waveguide to propagate the high frequency oceanic S_n phase was made by Isacks and Barazangi[10]. Their model consists of a transformation of the basaltic oceanic crust to a thin, high velocity, eclogite layer as the slab descends to greater depths. Thus the upper flank of the slab provides an effective reflecting surface and, in combination with a velocity gradient within the slab, could provide an efficient waveguide for the propagation of high frequency seismic energy.

SUMMARY

The model of the propagation of P_n presented consists of an arrival confined to the oceanic lithosphere with subsequent water and sediment reverberations comprising the

ensuing wavetrain. The low spatial attenuation observed for P_n does not require an intrinsically high Q lithosphere waveguide but rather can be explained in terms of the extremely high Q in the oceanic water column. The depletion of high frequencies in the normal refracted arrival relative to P_n is due to propagation through the low Q asthenosphere.

REFERENCES

1. D. Walker, High-frequency P_n and S_n phases recorded in the western Pacific, *J. Geophys. Res.* 82:3350 (1977).

2. R. Apsel, Ph. D. thesis, University of California, San Diego, La Jolla, 349 pp. (1979).

3. J. F. Gettrust and L. N. Frazer, A computer model study of the propagation of the long-range PN phase, *Geophys. Res. Lett.* 8:749 (1981).

4. R. H. Johnson and R. A. Norris, T-wave generation mechanisms, *Hawaii Institute of Geophysics Rept. HIG-70-7*, 16 pp. (1970).

5. K. Aki and P. G. Richards, "Quantitative Seismology: Theory and Methods," W. H. Freeman, San Francisco (1980).

6. I. I. Kim, D. K. Smith, J. A. Orcutt, T. H. Jordan and H. W. Menard, Seismic reflection site survey: correlation with physical properties, leg 91, Deep Sea Drilling Project, *Initial Rep. Deep Sea Drill. Proj., Leg* 91 (1985).

7. D. Walker, High-frequency PN,SN velocities: some comparisons for the western, central and south Pacific, *Geophys. Res. Lett.* 8:207 (1981).

8. W. H. Menke and P. G. Richards, Crust-mantle whispering gallery phases: a deterministic model of teleseismic P_n wave propagation, *J. Geophys. Res.* 85:5416 (1980).

9. G. V. Latham and G. H. Sutton, Seismic measurements of the ocean floor, *J. Geophys. Res.* 71:2545 (1966).

10. B. L. Isacks and M. Barazangi, High frequency shear waves guided by a continuous lithosphere descending beneath western South America, *Geophys. J. R. astr. Soc.* 33:129 (1973).
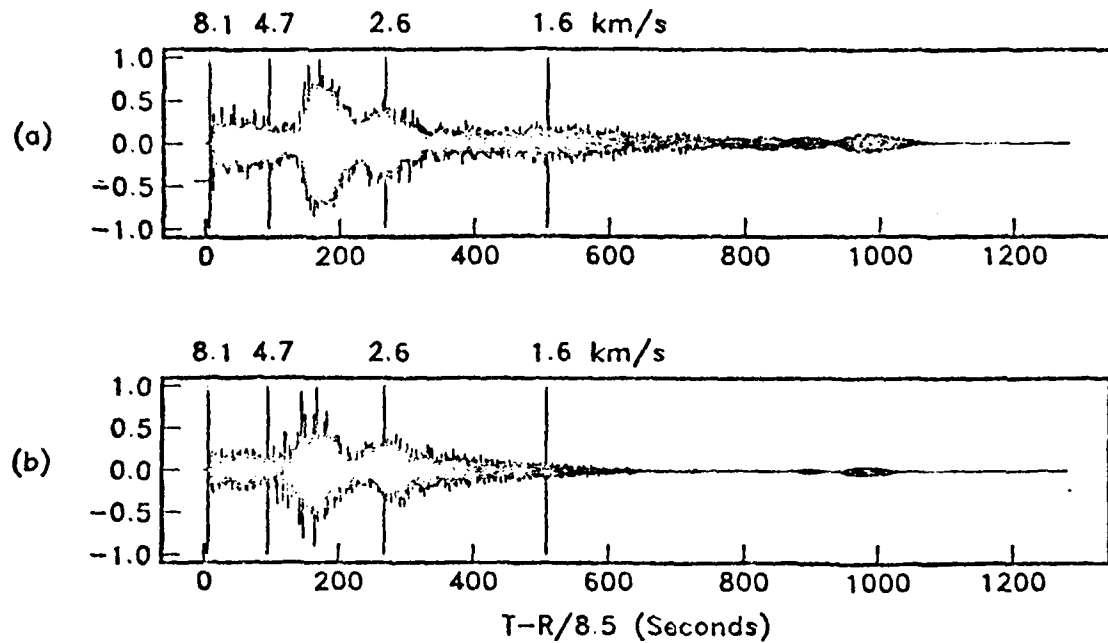
Figure 1. Complete synthetic seismograms at an epicentral range of 1000 km for a thrust fault source at 14.0 km depth. The fault had a dip of 45°, a rake of 270° and an azimuth relative to the receiver of 60°. (a) Vertical component and (b) horizontal component rotated 25° clockwise from the radial direction. Group velocities of 8.1, 4.7, 2.6, and 1.6 km/s are indicated. Phase velocities between 3.85 and 25.0 km/s were included in the calculation.
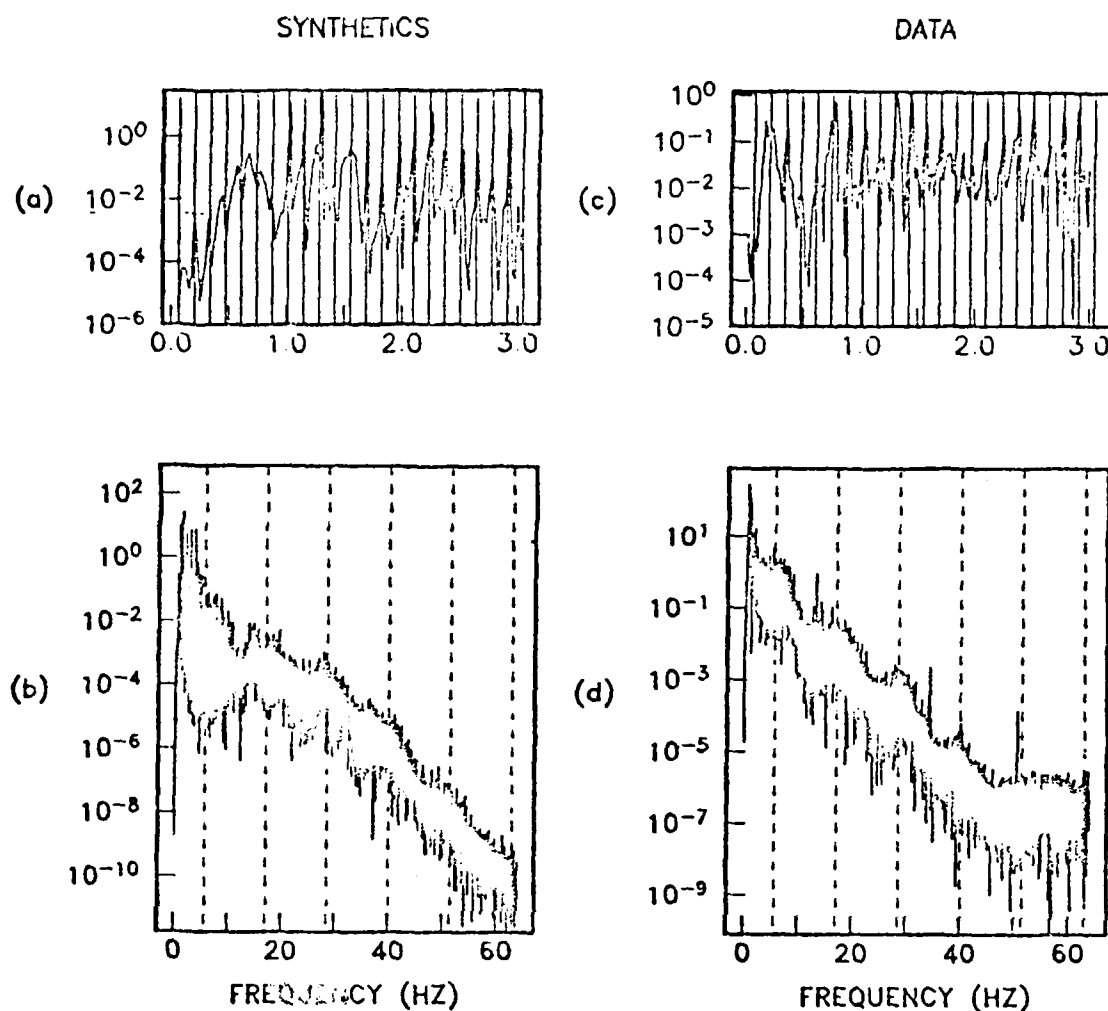
SYNTHETICS

DATA

Figure 2. Power spectra illustrating the presence of reverberation within the P_n coda.

(a) First 3.0 Hz of the synthetic vertical component spectrum depicted in (b).

(c) First 3.0 Hz of a hydrophone spectrum and (d) a complete OBS vertical

component spectrum. In figures (a) and (c) vertical lines indicate predicted

eigenfrequencies associated with water reverberation (equation (1)). In figures

(b) and (d) vertical lines indicate predicted eigenfrequencies for P-wave sedi-

ment reverberation.
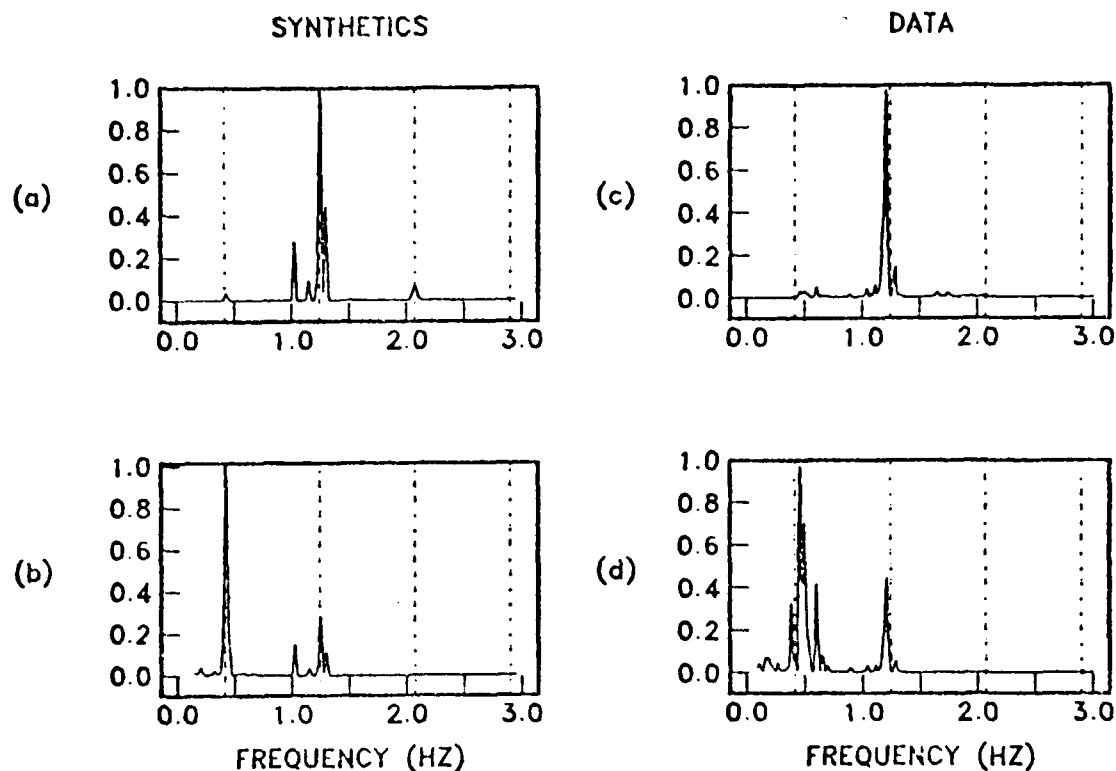
Figure 3. Power spectra illustrating shear wave sediment reverberations within the P_n coda. (a) First 3.0 Hz of the synthetic horizontal spectrum after including the instrument response and source spectrum. (b) Synthetic spectrum of (a) without including the instrument response. Power spectra of horizontal component data taken at the Ngendei site (c) before removing the instrument response and (d) after removing the instrument response. In (a)-(d), dashed vertical lines indicate predicted eigenfrequencies of S-wave sediment reverberation. The peak amplitudes in each figure were scaled to a value of one.
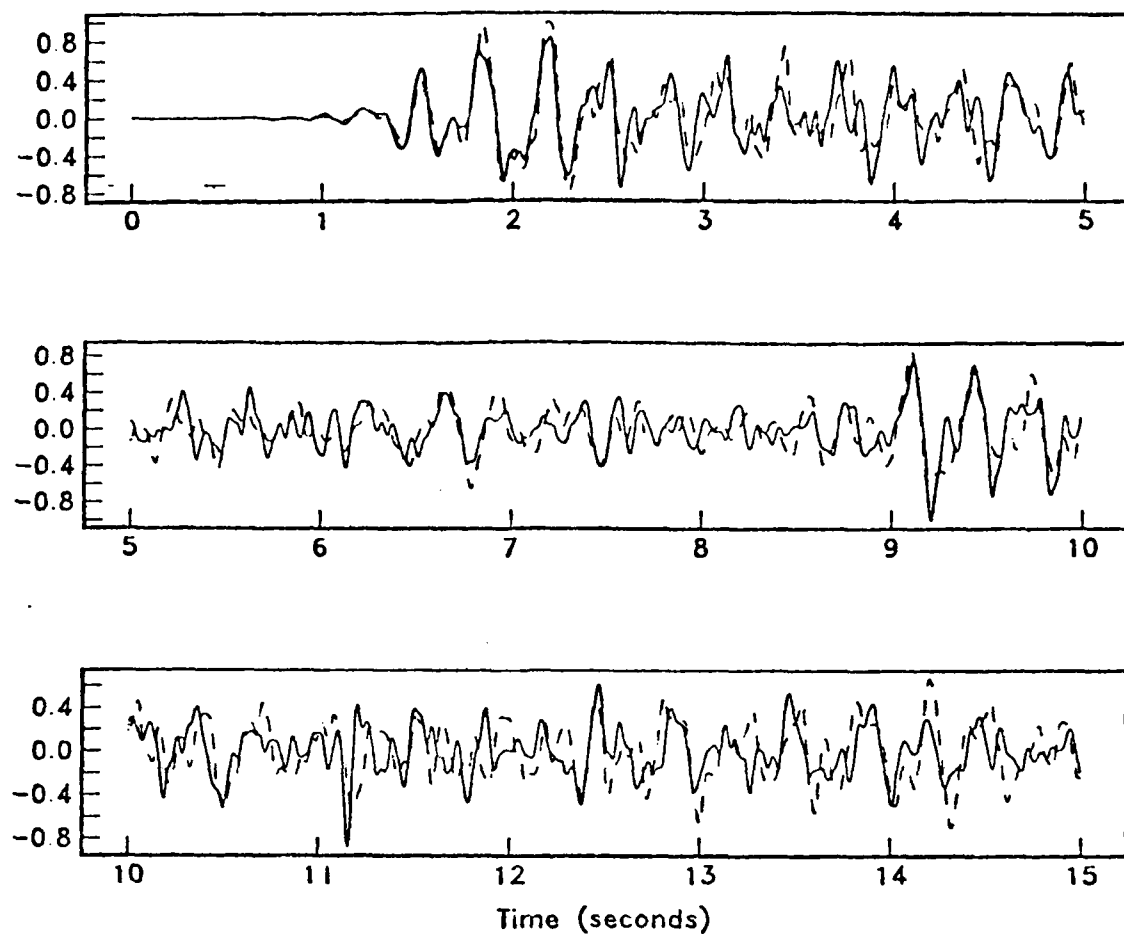
Figure 4. Coherence of the oceanic P_n phase. Comparison of recordings of the same event taken by OBS's separated by a distance of 1.9 km. OBS Karen (solid) vs. OBS Janice (dashed). The records were bandpassed between 2.0 and 25.0 Hz prior to comparison.
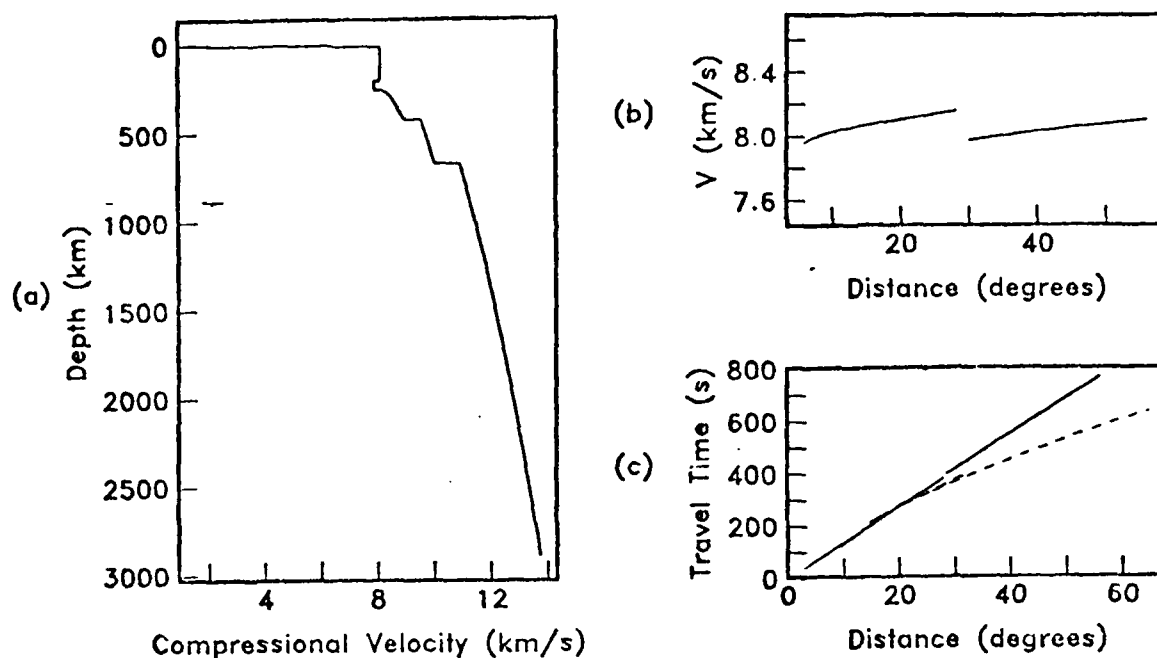
Figure 5. (a) Velocity model used to compute group velocities and travel times of P_n and normally refracted P. The results are shown for a surface source and receiver. (b) Group velocity of P_n as a function of epicentral distance for the model in (a). Group velocity has been defined as epicentral distance divided by total travel time. The discontinuous break at 30° represents the crossover between a ray normally refracted in the lithosphere and one that contains a free surface reflection. (c) Travel time curve of P_n (solid) verses normal refracted P with turning points below the base of the lithosphere (dashed) for the model in (a).
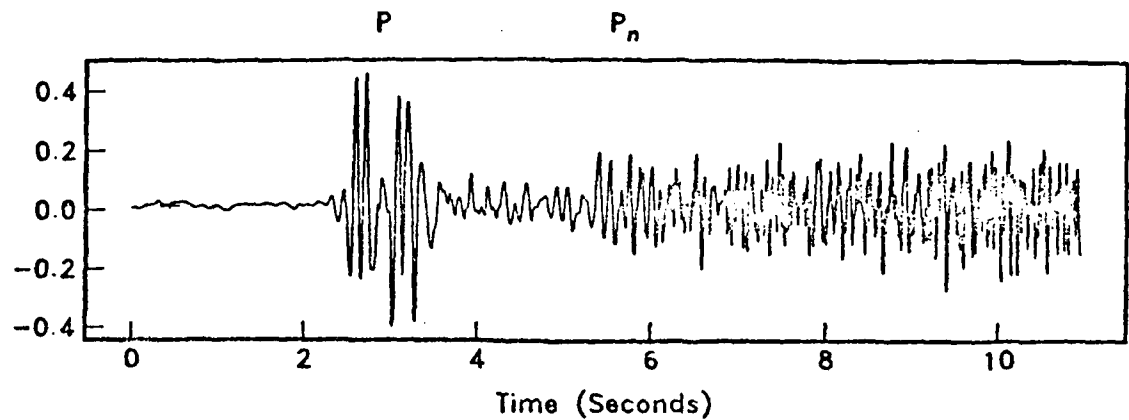
Figure 6. Vertical component seismogram recorded by a borehole seismometer at the Ngendei site. The focal depth of the event was 293 km in the Kermadec trench (m_b = 5.0, Δ = 12.91°). The complex P waveform between 2 and 4 seconds is a triplication from the 400 km discontinuity. Arrivals following 5.5 seconds constitute the P_n arrival. The enrichment in high frequency content of P_n relative to P is indicative of the low Q of the sub-lithosphere mantle.

CHAPTER 2

Ocean-bottom infrasonic, and ocean-bottom and sub-bottom seismic noise observations in the deep sea: Results from the Ngendei Experiment

Richard G. Adair and John A. Orcutt
Institute of Geophysics and Planetary Physics
Scripps Institution of Oceanography
La Jolla, California 92093

Thomas H. Jordan
Department of Earth, Atmospheric, and Planetary Sciences
Massachusetts Institute of Technology
Cambridge, Massachusetts 02139

ABSTRACT

Simultaneous measurements of ocean-bottom infrasonic, and ocean-bottom and sub-bottom seismic noise in the frequency band 0.1 - 20 Hz are presented. The data were obtained in 5.5 km-deep water in the South Central Pacific with a triaxial borehole seismograph and six triaxial ocean-bottom seismographs having externally-mounted hydrophones. The borehole sensors were emplaced 50 meters within basement rock overlain by 70 meters of pelagic clay. In the band 0.1 - 1 Hz, noise propagation as seismic modes trapped near the seafloor is supported by observed spectral coherences, cross-phases, and ratios between ocean-bottom pressure and vertical ground motion, and by the relatively lower noise levels in the borehole. Noise variations in this band are clearly correlated with changes in local wind direction and speed, presumably through ocean-bottom pressure fluctuations caused by nonlinear wind wave-wind wave and wind wave-swell interaction.

INTRODUCTION

In considering the response of the coupled ocean-seafloor elastic system, one must inescapably conclude that ocean-bottom seismic and infrasonic noise are related in source and character. This relationship is confirmed by observations of these two types of ambient noise. Measurements of seismic noise at the ocean bottom reveal the presence of the ubiquitous microseism peak (actually an agglomeration of peaks) over the microseism band (periods between 1 - 10 seconds) (Bradner et al.[1] and Latham and Sutton[2]). Ocean-bottom pressure measurements of high resolution over the microseism band, of which very few are published (Latham et al.[3], Nichols[4], and Cox et al.[5]) also display the microseism peak. Observed amplitude and phase relationships between the ocean-bottom pressure and vertical-component seismic noise are consistent with those of normal modes trapped near the ocean-seafloor interface (Latham and Nowroozi[6]).

Over the microseism band an, intimate relationship between microseismic noise and non-linear surface gravity wave interactions has been both hypothesized (Longuet-Higgins[7] and Hasselmann[8]) and observed (Haubrich et al.[9], Latham and Sutton[2], Kibblewhite and Ewan[10] and Cox et al.[5]). This non-linear interaction occurs between opposed gravity waves of the same period and produces ocean-bottom pressures fluctutions of half the gravity wave period. The microseism peaks are the manifestation of this phenomonenon.

Although regional swell is most frequently identified as the primary source of microseisms in the deep ocean, recent observations have emphasized the role played by local wind-generated waves (Kibblewhite and Ewan[10]). Hasselmann[8] predicts a spectral form for ocean-bottom pressure fluctutations $\propto f^3 S^2(f/2)$ at frequency f, where S(f) is the gravity wave spectrum. The asymptotic form of wind-generated waves is $S(f) \propto f^{-5}$ (Pierson and Moskowitz[11], Hasselmann et al.[12]) or, in some circumstances, f^{-4} (Kahma[13]). Thus, a fall-off $\propto f^{-5}-f^{-7}$ would be expected and, in fact, is observed (Cox et al.[5], Latham et al.[3], Figure 6, and Nichols[4]).

This paper presents ocean-bottom and sub-bottom observations from a recent ambient noise experiment in the South Central Pacific in which the dominant mechanism of ambient noise generation was clearly wind-related. The

growth of spectral peaks and generally increased levels over the microseism band in both seismic and acoustic measurements followed sharp changes in wind direction. Activity in the microseism band abated as the wind persisted or died away. Amplitude and phase relationships between pressure and vertical seismic motion at the microseism periods imply that the a portion of the noise propagated as trapped modes of the ocean-seafloor elastic system. The appearance of peaks at periods corresponding to acoustic reverberations in the water-sediment column suggests that some of the ambient noise may be due to (leaky) organ-pipe modes.

These observations constitute the first comparison of simultaneous ocean-bottom and sub-bottom seismic noise and ocean-bottom acoustic noise over the microseism band in the deep ocean.

I. EXPERIMENT DESCRIPTION

The Defense Advanced Research Projects Agency (DARPA) developed a marine borehole seismograph, the Marine Seismic System (MSS), for seismic discrimination applications. The successful test of an MSS prototype tethered to the D/V Glomar *Challenger* on Deep Sea Drilling Project (DSDP) Leg 78B (Ballard et al.[14]) led to deployment of the fully-operational MSS on DSDP Leg 91, which composed the first portion of the Ngendei Experiment.

A primary objective of the Ngendei Experiment was the appraisal of the relative seismic signal and noise characteristics at a marine borehole site and proximate ocean-bottom site. This behavior was at issue because the first generation of ocean-bottom seismograph (OBS) efforts during the 1960's revealed that ambient seismic noise levels in the microseism band were typically 10-20 dB higher at ocean-bottom sites than at nearby land sites. In the microseism band, seismic noise at land sites is dominated by fundamental mode surface waves, the amplitude of which diminishes with depth into more rigid basement rock (Sorrells[15]). Since marine seismic noise is similarly composed, it was thought that the same advantage might obtain at a marine borehole site over an ocean-bottom site.

The MSS sensors were deployed in DSDP Hole 595B, located midway between New Zealand and Tahiti at 28° 49.34′ S,165° 31.61′ W. Further details of the Ngendei Experiment may be found in Volume 88/91 of the Initial Reports of the DSDP.

II. INSTRUMENTATION AND OPERATIONS

A. Ocean Bottom Seismographs

The six OBS's are modifications of the four-component, digital event-recorders described by Moore et al.[16] (Orcutt et al.[17]). Output from three components of ground motion (one vertical and two horizontal) and a hydrophone are amplified, bandpassed, and digitized with a 12-bit word at 128 samples/second (s/s). The gain of each channel is 2^N, where N=0,1,...,9. A channel's gain exponent N is modified only when the long-term average of its digital output, corrected for DC offset, falls outside pre-defined bounds of a few least significant bits.

Semiconductor memory, nominally 13-seconds long per channel, continuously accumulates the four channel data in a cyclically overwritten buffer to avoid the mechanical shaking and electrical transients of recorder operation. Software writes events to tape at scheduled times or when the short term average of vertical component amplitudes exceeds a long term average threshold. Additional RAM boards extended the 13-second buffers of several OBS's to 59 seconds.

The OBS's employed two seismometer responses *(see Figure 1a)*, selectable only prior to deployment. The 'teleseismic' response emphasizes lower frequencies more than the 'refraction' response in order to increase the sensitivity of the OBS event-triggering algorithm to moderate-amplitude, high-frequency depleted earthquake signals. The 'refraction' and 'teleseismic' capsules employed the same

hydrophone response (*Figure 1a*).

The seismometers are the 1-Hz free period Mark Products L-4-3D triaxial set, and the hydrophone is an Ocean and Atmospheric Sciences, Inc., model E-2PD deep-water sensor. A bouyant aluminum sphere mounted on a detachable, dish-footed tripod houses the OBS instrumentation. Explosive bolts, detonated either by an acoustic or programmed command, free the instrumentation sphere, which then floats to the surface for recovery.

B. Marine Seismic System

The MSS comprises a borehole instrumentation package (BIP) connected by coaxial cable to either an ocean-bottom recording unit, known as the Bottom Processing Package (BPP), or to two shipboard recording systems employed for diagnostic checkout and recording redundancy. One of the shipboard recording systems, referred to as the Teledyne system, specifically monitors the borehole package, while the other, the Gould system, emulates the BPP. A special tool at the end of the drill string carries the sensor package to the seafloor, although simple lowering of the mechanically-strong coaxial cable, 'wireline' deployment, provides an alternate means to achieve this end. To date, only drill string deployments have been employed, although successful recovery of the BIP has been achieved by wireline.

The borehole sensors are four Teledyne Model S-750's configured as a primary triple (orthogonal horizontals, X and Y, and one vertical Z) and a backup vertical component (B). The backup sensor B is located 175.5 cm below the primary vertical sensor Z. Output from the three primary sensors X, Y, and Z are filtered in mid-period (MP) and short-period (SP) bands, while output from the backup sensor B is passed through the SP band only. The MP and SP transfer functions are shown in *Figure 1b*. The resultant seven data streams are then digitized and transmitted to recording devices via the coaxial cable.

Data recorded on the Teledyne system are continuously gain-ranged to yield a 21-bit dynamic range with 14-bit resolution. No low-pass filter is employed other than the roll-off of the instrument response. The MP and SP bands are digitized at 4 and 40 s/s, respectively, although either of the two SP vertical channels may be digitized at 80 s/s to the exclusion of the other.

Output recorded by the BPP and its shipboard counterpart are oversampled 256-fold, transmitted, digitally-convolved with a low-pass filter, resampled at the proper rates of 4 s/s and 40 s/s for the MP and SP bands, respectively, and buffered to tape as 24-bit integers with 24-bit resolution. The transfer function of the digital low-pass filter is nearly flat to 75% of the Nyquist frequency, and thereafter falls at approximately 720 dB/decade. The low-pass filter coefficients are the same for both passbands. The dashed lines in *Figure 1b* illustrate the augmentation due to the low-pass filter

C. Operations

The first 20 days of the 60-day long Ngendei Experiment comprised a seismic refraction experiment, during which the OBS's recorded refraction signals and teleseismic signals with two distinct arrays, and the MSS operated with its two shipboard systems. The remaining 40 days were devoted to a teleseismic experiment during which the OBS's formed a single array for earthquake and noise recording, and the MSS employed its ocean-bottom recording system.

The D/V Glomar *Challenger* conducted MSS installation and shipboard recording operations. The Scripps Institution of Oceanography R/V *Melville* tended the six OBS's and recovered all instrumentation. *Figures 2* and *3* show instrumentation locations throughout the experiment. In these figures, octogons centered on ellipses depict estimated OBS locations and their 95% confidence bounds based on least-squares modeling of satellite and acoustic ranging data (Creager and Dorman[18]). Diamonds and arrows denote OBS drop points computed from satellite navagation and *Melville* radar ranging of *Challenger*. The borehole location is computed relative to the best satellite fix of *Challenger's* location.

During the refraction experiment, four OBS's were placed 0.6-0.7 km from the MSS site *(Figure 2a)*, and two at approximately 30 km *(Figure 2b)*. The former quartet of capsules employed the 'refraction' seismic response, 13-second event memory, and scheduled event recording, while the latter pair employed the 'teleseismic' response, 59-second event memory, and triggered event recording with scheduled noise samples at three-hour intervals.

The BIP rested unclamped at the bottom of DSDP Hole 595B, approximately 50 meters within a basaltic basement overlain by a 70-meter thick layer of zeolitic pelagic clays bearing hard stringers of porcellanite and chert near its base. The BIP holelock/cable isolation mechanism damaged the coaxial cable during an aborted deployment and was subseqeuntly discarded. Comparison of MSS and OBS waveforms indicate that MSS sensor coupling with the ground was adequate. A coil of the coaxial cable payed out on the seafloor aided in cable-motion isolation.

During the teleseismic experiment, the six OBS's were redeployed in a triangular array with single capsules forming two 25-km legs at approximate right-angles to the south and east of the MSS site *(Figure 3a)*. The other four capsules were clustered within 3 km to the west and north of the MSS in a trapeziform array *(Figure 3b)*. All OBS's employed the 'teleseismic' response, and triggered event recording, two with 13-second memory buffers and four with 59-second buffers. Daily noise events were recorded at Universal Time (UT) midnight. The MSS ocean-bottom recording system failed two days after entering the water due to a water leak.

Successful recovery of all OBS's and the MSS recording system took place from *Melville* over the period 22-26 March, 1983. Following a two-day shipboard recording period, the MSS recovery mooring was redeployed with a dummy load to replace the recording system. Both BIP and recovery mooring are still in place for future use.

III. NOISE DATA

Totals of 119, 43, and 83 hours of seismic data were obtained from the Teledyne system, the Gould ocean-bottom recording system, and its shipboard counterpart, respectively. During the refraction experiment, 114 and 70 hours of shipboard data were recorded on the Teledyne and Gould systems, respectively. OBS's recorded a total of 1400 noise events at 740 distinct times, 140 concurrently with MSS data.

Various MSS data channels were unavailable at certain times. The horizontal sensor Y malfunctioned throughout the entire Ngendei experiment for unknown reasons and provided no usable data. A shipboard source of electrical interference contaminated the subsequently-disconnected Gould channel SZ. A Gould electronics failure in its BIP bay disabled Gould channel MZ at the start of the teleseismic experiment. Finally, as mentioned above, one of the Teledyne SP Z channels was not available whenever the other recorded at 80 s/s.

IV. DATA QUALITY

Data quality was assessed with both time- and frequency-domain criteria, the latter applied to power, cross, and coherence spectra.

Reliable spectral estimates were computed in the manner described by Welch[19] and Carter et al.[20]. Non-overlapping, de-meaned segments of digital data were tapered with a normalized Hanning window and Fourier transformed. The resulting spectra were averaged to achieve a reduction of estimate variance. Power spectra, defined only for non-negative frequencies, are normalized so that the total power in the Nyquist-frequency bandwidth equals the time-domain variance, a normalization which essentially folds the power of negative frequencies into the positive.

Estimates of statistical reliability were calculated under the assumption that the data derived from a stationary, Gaussian stochastic process. Power spectral estimates are then distributed as χ^2 random variables with 2N degrees of freedom, where N is the number of spectra averaged to obtain the estimate (see, e.g. Bendat and Piersol[21]).

The complicated statistics of the magnitude-squared coherence, here termed coherence for conciseness, are essentially those of the linear-regression correlation coefficient (Carter et al.[20]; Fischer[22]). The coherence's cumulative probability function simplifies greatly if the actual coherence C is zero, from which the coherence R at which an estimate $\hat{C}$ is significantly different from zero for a given significance level is easily determined. This is inferred from

$$P(\hat{C} < R \mid C = 0) = 1 - (1 - R)^{N-1}, \tag{1}$$

where $P(--)$ is the probability that the estimate $\hat{C}$ does not exceed the value R given the the actual coherence C and N is the number of spectra averaged in the coherence estimate. Thus, the threshold coherence R is given at the 100P % confidence level by

$$R = 1 - (1 - P)^{\frac{1}{N-1}}. \tag{2}$$

In computing spectral estimates from OBS data, the number of spectra averaged, and stationarity must trade-off because OBS noise samples are available only at discrete times: N must be large enough to yield estimate stability and useful error bounds, but not so large as to sample over a time interval such that the noise field has statistically evolved. N=10, a 30-90 minute interval, was found to be generally optimal. This trade-off is not very important for MSS data since they were continuously recorded except during brief interuptions. However, where comparisons of simultaneous observations are desired, the statistics and frequency resolution of the MSS estimates were made similar to those of the OBS.

Linear regressions of Gould data against Teledyne data in conjunction with sensor calibrations revealed a 3 dB shortfall of Gould amplitudes. The calibrations also show that instrument response below 0.2 Hz is not good for any MSS channel.

Figure 4 compares power spectral density estimates of simultaneous vertical-component Teledyne and Gould data with instrument noise spectra which have not been corrected for instrument response. The peaks above 8 Hz in the SB spectra are ship-generated. Peaks in the SB Teledyne spectrum *(Figure 4c)* which are absent in the SB Gould spectrum *(Figure 4b)* are manifestations of aliasing in the Teledyne data due to inadequate high-frequency filtering. Gould and Teledyne spectra have comparable values near the Nyquist frequency, indicating probable malfunctioning of Gould's low-pass filter.

Also shown in *Figure 4* are estimates of system noise, provided by H. B. Durham of Sandia Laboratories. The system noise is not significant over the entire SP passband for either Teledyne or Gould data. The flat spectrum of quantizing noise for the Teledyne data, associated with uniformly-distributed round-off errors of digital representation (see e.g. Bendat and Piersol[21] pp. 231-232), has a level near 10^{-2} counts^2/Hz, well below the Teledyne signal level. Estimates of Gould's digitizing noise spectrum, that of a delta modulator, are not available. The MZ spectrum *(Figure 4a)* is similarly untainted by system and sampling noise. The MZ instrument response rolls-off sufficiently at high frequencies to avoid aliasing.

Spectral coherences *(Figure 5)* further delineate frequencies usable for ambient noise estimates. Coherences exceeding 0.28, illustrated in *Figure 5*, with a dash line, are considered significant at the 95 % level. MP coherences *(Figure 5a)* typically exceed 0.95 below the low-pass filter knee at 1.5 Hz except at 1 Hz, where it drops sharply over a very narrow band of frequencies. The sharp drop is due to energy present in the Gould data but not the Teledyne, and may be related to the Gould digitizing scheme. Gould and Teledyne SB coherences *(Figure 5b)* exceeds 0.8 between approximately 0.2 and 4.0 Hz. The coherence at higher frequencies declines amidst peaks due to ship-generated signals. The sharp drops at approximately 2 and 4 Hz are similar to that at 1 Hz in the MP coherence. The frequencies bounding the SP band of high coherence varied a great deal during the MSS deployment, but generally were those shown in *Figure 5*. Coherence estimates between SB and SZ Teledyne data *(Figure 5c)* were similar. Differences at frequencies greater than 4 Hz are probably due to the combined effects of aliasing and actual signal differences over the 175.5-cm sensor

separation. The high coherence between the Gould and Teledyne data at the Nyquist frequencies indicates a possible deficiancy in the Gould low-pass filtering scheme.

OBS's employing the refraction response can measure lower-amplitude ground motion at high frequencies than those employing the teleseismic response. The refraction response was specifically designed to 'whiten' the ambient signal in the presence of typical deep-sea microseismic noise (Moore et al.[16]), while the teleseismic response was designed to low-pass it. Filtered high-frequency amplitudes are consequently less than that represented by a least significant bit as recorded with the teleseismic response. *Figure 6* compares spectra measured with the different OBS responses (upper curves) and shows the corresponding spectra of least-count noise (lower curves). The spectra, corrected for instrument response, were not measured simultaneously. Although most of the data composing the teleseismic capsule's spectrum (solid upper curve) were recorded after ship departure, their spectral levels exceed ship noise levels measured with a refraction capsule (dashed lower curve) at most frequencies. In the teleseismic spectrum, sampling noise clearly dominates at frequencies greater than 15 Hz, and is probably significant in the range 7-18 Hz.

The lowest valid frequency of OBS microseismic measurements is taken to be 0.1 Hz. At lower frequencies, least-count and system noise dominate. The system noise was inferred from the lack of estimate stability over a wide range of numbers of spectra averaged to compute power density estimates.

Ship-generated noise must be estimated on a case-by-case basis because it depends on ship speed, activity and range. Generally, sharply distinct peaks superimposed on a broadband level characterize ship-generated noise. In the Ngendei data, most peak frequencies appear to be multiples of some fundamental, indicating that propellor cavitation caused the peaks (e.g. Urick[23]). *Challenger* generated peaks at multiples of 10 Hz while maintaining station, and two others at approximately 6.5 and 7.5 Hz while under way. *Melville* generated peaks at multiples of 6 and 9 Hz. *Figure 7* shows the growth of a peak at 18 Hz due to *Melville's* proximity to the MSS.

Figure 8a illustrates ship-generated noise with a comparison of vertical-component power density spectra, corrected for gain but not instrument response, of OBS Phred data recorded before (solid curve) and after (dashed curve) both ships departed. The capsule, located 1.6 km west of the borehole, employed the teleseismic response. The measurement prior to ship departure was made as both *Challenger* and *Melville* hove to within 2 km of the OBS. In this instance, ship-generated noise clearly dominates the spectrum at all frequencies above approximately 4.5 Hz. After ship departure, least-count noise dominated above 7 Hz, although the lowest frequency at which it dominated varied by ± 1 Hz since the level depends on OBS gain.

Some ambiguity exists concerning ship noise in the MSS data. Because the BPP failed two days after its deployment when *Challenger* was 13 km away drilling Hole 596 and *Melville* was en route to Tahiti, MSS noise measurements in the complete absence of ships are not available. However, *Challenger* was briefly silent c 0510Z, 13 Feb, while monitoring an ocean- bottom navigational

transponder, thus providing a sample of low ship noise for the MSS. *Figure 8b* compares the MSS spectrum of this time period with that measured a short time later when *Challenger* began using its dynamic positioning system thrusters. Also shown in *Figure 8b* is an estimate of SP system noise which has been scaled to fit the 'quiet' spectrum. The good fit suggests that above 7 Hz system noise dominates the spectrum.

The dominance of ship-generated noise is in many instances diagnosed by an abrupt change in spectral slope, such as is seen in *Figure 8* at approximately 4 Hz. On this basis, it is apparent from these and other spectra that ship noise may be important at frequencies as low as 2 or 3 Hz in both the OBS and MSS data.

In summary, reliable spectral estimates of ambient seismic noise are available from MSS MP data between 0.2 and 1.5 Hz; from MSS SP data between 0.2 and 7 Hz; and from OBS data between 0.1 and 7 Hz. These bands are subject to the variability described above due to ship proximity, and OBS gain range and instrument response. At frequencies greater than 7 Hz, sampling noise dominates OBS teleseismic data, so that lower bounds on ocean-bottom microseismic noise levels must be established using data recorded with the refraction response.

V. RESULTS AND DISCUSSION

Figures 9 - 12 compare displacement power densities for all available components, in units of nanometers²/ Hz (nm²/ Hz) for simultaneous MSS and OBS data. The data were obtained at 5- and 10-minute intervals over a 70-minute period. Spectra are averages of 10 individual spectra obtained from approximately 13-seconds of data. The OBS, Suzy, was 0.6 km north of the MSS site. Based on considerations mentioned above, ship noise is assumed to dominate these spectra above 4 Hz.

The spectra all display the ubiquitous microseism peak near 0.2 Hz, where the observed noise levels are comparable, approximately 10^8 nm²/ Hz. At higher frequencies, ambient ocean-bottom microseismic noise levels exceed the borehole levels by 5-30 dB *(Figures 9 and 10)*. Common to the spectra, though not prominent in all of the OBS spectra, are peaks centered on 0.5 and 0.7 Hz. At the ocean bottom, horizontal levels exceed the vertical levels at all frequencies greater than that of the microseism peak and display a character quite different from that of the vertical component between 0.3 and 0.6 Hz *(Figure 11)*. In contrast, the borehole vertical-component spectrum uniformly exceeds the horizontal-component spectrum by an insignificant amount (4 dB) over the entire frequency band *(Figure 12)*. These observations are consistent with the propagation of noise as a fundamental mode interface wave with large vertical and horizontal displacements at the interface and lower amplitudes at depth in more rigid rock. The comparable levels at the microseism peak suggest that the amplitude of the trapped waves are still significant at the depth of the borehole sensor.

The ocean-bottom pressure spectrum measured simultaneously with the above spectra also displays the microseism peak *(Figure 13)*. The fall-off towards higher frequencies decreases with frequency from the microseism peak. Between 0.2 and 0.7 it falls at 100 dB/decade; between 0.7 and 2 Hz at 54 dB/decade; and above 2 Hz at 27 dB/decade, where ship noise evidently dominates.

The microseism peak and a 0.4 Hz-wide band centered at 1 Hz display high coherence and a cross-phase of approximately 180° *(Figure 14 (a) and (b))* between the pressure and vertical displacement. It may be shown that at a fluid-solid interface, kinematic boundary conditions require a 180° phase shift for both normally-incident plane waves reverberating in the water column (Bradner[24], and Schneider and Backus[25]) and for trapped modes of the ocean-seafloor elastic system, the gravest of which is confined near the interface at these frequencies (Latham and Nowroozi[6], and Latham and Sutton[2]). For plane waves, the pressure-seismic velocity ratio is constant with frequency and equals the product of density ρ and acoustic speed α in the water, 1.5×10^6 in MKS units, while for normal modes it may vary with frequency and exceed $\rho \alpha$ (Latham et al.[3] and Latham and Nowroozi[6]). *Figure 14 (c)* plots the ratio between the pressure and vertical-component velocity power density spectra, normalized by $(\rho \alpha)^2$. Over the two bands of high coherence, this ratio is on the order of 10, rather than one, suggesting that in this instance they represent trapped seismic modes. Thus, in this case the practice of comparing seismic ground velocities $V(f)$ to a 'plane-wave equivalent' pressure $P(f)$ via the relation $P = \rho c V$ is incorrect.

Figures 15-16 shows the coherence and cross-phase between the vertical and hydrophone channels of OBSs Suzy and Lynn, seperated by 0.6 km, for the same time interval as above. Again, energy at the microseism peak is highly coherent. The cross-phase at these frequencies is not significantly different from zero, implying either simultaneous arrival of microseism energy at the two capsules or a wavelength much larger that the capsule seperation. Latham et al.[6] calculate the dispersion for normal modes in an ocean-bottom structure similar to that of the Ngendei site. At these frequencies the fundamental mode has a phase velocity C_p of 1.0 - 1.5 km/s, corresponding to a wavelength $\lambda = C_p/f$ on the order of 5 km. The capsule separation, roughly $\lambda/10$, is too large to account for the observed small cross-phases, which rules-out oblique arrival of the microseism energy from a distant source. It therefore appears that the microseism source location in this instance is either local or along a line that is approximately normal to a line defined by the OBSs.

Evidence abounds that the sea state affects microseismic and infrasonic noise levels. The non-linear interaction of opposed ocean surface waves of a given frequency generate substantial ocean-bottom pressure fluctuations of twice the waves' frequency (Longuet-Higgins[7] and Hasselmann[8]). This has been conclusively demonstrated for swell reflected from a shoreline (Haubrich et al.[9]), and for wind-waves (Kibblewhite and Ewan[10]; Webb[26]). Decklog observations provide observations pertinent to local and distant noise source discrimination. *Figure 19* summarizes *Challenger* decklog observations of wind and swell between 24 January and 13 February, 1983 (Julian dates 24-44) at two-hour intervals except for 8-10 hours swell gaps corresponding to local nighttime, and for hourly observations during days 33-37. The prevalent swell arrived from the south and had 6-7 second periods. The highest-amplitude swell had periods between 8-10 seconds, predominantly 9 seconds, and arrived from the south between dates 29-31 and 34-35. Very little northerly swell was observed. The wind direction

changed both suddenly and gradually, the latter being marked by smooth changes in wind speed.

Figure 18 shows the variation of OBS Phred vertical-component acceleration spectra with time at three-hour intervals except for gaps due to triggered event recording. The spectra, single realizations corrected for instrument response, are computed from 58 seconds of data. The noise clearly changes with time, particularly at the prominent peaks near 0.2 and 0.5 Hz, which have comparable levels. *Figure 18(b)* plots the time-variation of the power in a 0.2 Hz band centered on these peaks, along with wind (*Figure 19(a)*) and swell (*Figure 19(c)*) observations over the same period. Abrupt increases in the power of both peaks, e.g. days 28.0, 30.0 and 33.0, coincide in several instances with sudden changes in wind direction. The onset of high-amplitude 9-second swell coincides with the wind change and power increases at day 30.0, but opposing 9-second swell, probably masked by other swell, were not observed. The onset at day 33 of the high-speed wind episode from the SSE coincides with a large power transient of the 0.5 Hz peak and a gradual ramping of power of the 0.2 Hz peak. Noise observations of 13-seconds length collected at three-minute intervals from the 'refraction' OBS's near the MSS site during day 33 show the peak at 0.5 Hz building quickly over the course of an hour. Power for both peaks gradually diminished as the wind weakened and wound northward. OBS Phred pressure spectra varied similarly with time. The clearly correlated behavior of the ambient noise and the wind as a major source of microseisms.

The observed variations of the wind are clearly related to those of the noise in *Figure 19*. A sharp change in the wind vector immediately preceeds, to within the 2-hour resolution of the decklog, noise increases at frequencies greater than the microseism peak band. Hasselmann[8] shows that the direct conveyance of pressure from the atmosphere at these frequencies is unlikely, leaving only the non-linear interaction of wind-generated gravity waves or of wind-waves with background swell as a likely source for the seismic variations. In the case of wind wave interaction only, Hasselmann[8] derives the following expression for the spectral density $S_P(f)$ of the ocean-bottom pressure fluctuations at frequency f:

$$S_P(2f) = 8\pi \frac{\rho^2 g^2}{c^2} \omega^3 S_W^2(f) \int_0^{2\pi} G(\theta) G(\theta + \pi) \, d\theta , \qquad (3)$$

where $\omega = 2\pi f$, $S_W(f)$ is the wave height power density, ρ and c are the density and sound speed of water, g is gravitational acceleration at sea level, and $G(\theta)$ is the angular dependence of the wind wave spectrum. $S_P(f)$ may be thought of as a forcing function for seismic wave generation. Note that the non-linear interaction between exactly-opposed waves of frequency f (cf the angular integrand in *Equation (3)*) leads to the double-frequency dependence 2f of the ocean-bottom pressure fluctuations. Implicit in *Equation (3)* is a white wavenumber spectrum which contributes only at phase speeds exceeding the sound speed of water, that is for wavenumbers $\leqslant \omega / c$.

A large body of observations (Pierson and Moskowitz[11]; Hasselmann et al.[12]) support self-similar form for the wind wave spectrum $S_W(f)$ of

$$S_W(f) \propto f^{-5} e^{-\frac{5}{4}(\frac{f_m}{f})^4}, \tag{4}$$

The function described in *Equation (4)* falls exponentially for $f \leqslant f_m$ and as f^{-5} for $f \gg f_m$, where f_m is the peak frequency. Empirically, f_m decreases and power density increases with time under the influence of a constant wind. Tyler et al.[27] found that $G(\theta)$ is adequately described by

$$\cos^q(\theta / 2), \tag{5}$$

where q is a function of frequency and $\theta = 0$ corresponds to the mean wind direction.

A more detailed view of this interplay may be obtained from the continuously-collected MSS data. *Figures 20 (a), (b)* show the temporal variation of mid-period vertical acceleration in the borehole using data from Teledyne channels MZ. Averages of 14 spectra computed from consecutive 128-second samples, nearly 30 minutes total data, form the individual spectra of *Figure 20*. The dominant feature of these spectra is the microseism peak near 0.2 Hz, which with time steadily migrated towards lower frequencies, and grew larger in amplitude and narrower in width. Note the 'saddle' in the peak's amplitudes near day 41 coinciding with with generally-increased levels at higher frequencies. In contrast to the ocean-bottom accelerations, levels at the 0.5 Hz peak *(Figure 18 (b))* are an order of magnitude lower than those at 0.2 Hz. Other peaks are observed at 0.35, 0.65, and 0.80 Hz *(Figure 20(b))*.

Figure 21(b) compares the temporal variation of power for the microseism ('primary') and 0.5 Hz ancillary peaks of *Figure 20*. Power was estimated by integrating over 0.10 Hz-wide bands centered on 0.22 and 0.50 Hz. Power variations in these two bands are roughly parallel until c. day 40.7, after which they were complimentary, corresponding to the microseism peak's 'saddle'. The power of these peaks decreased in an unknown manner early in the MSS shipboard recording period, then began growing c. day 39.0. Power in the ancillary band diminished during day 39, but resurged c. day 40.0. Power in both bands changed little in the half-day preceding day 40.7, then decreased in the primary band and increased in the ancillary band. At c. day 41.0, power leveled-off in the microseism peak band and generally increased at higher frequencies, which peaked c. day 41.2. The *rate* of power growth in the two bands increased c. day 41.5, so that primary power increased and ancillary power fall-off slowed. By the end of the shipboard recording period, power in both bands attained levels comparable to those observed c. day 40.5.

Figures 21 (a) and *(c)* show weather observations during the MSS shipboard data collection period, which began just as the epoch of the strongest winds observed during the Ngendei Experiment was concluding. Southerly swell of 6-7 second period dominated most of the time although northerwesterly swell briefly dominated c. day 41 *(Figure 21 (c))*. The wind, on the other hand, varied a great deal *(Figure 21 (a))*. A moderate northeasterly wind blew during most of days 37 and 38 at a nominal 10 knots. During day 39, the wind was confused, though still northeasterly. The wind blew northwesterly throughout day 40, and southwesterly for the rest of the shipboard recording period. The highest wind

speeds during the MSS shipboard recording period, 18 knots, accompanied the shift in wind direction from northwest to southwest at day 41.0.

The available data permit only a gross description of the sea. However, the forgoing discussion of wind-wave evolution permits drawing reasonable inferences of the wind-wave behavior from *Challenger* decklog observations. The increases in noise power at frequencies greater than those of the microseism band which follow soon after sharp changes in the wind vector are probably due to the wind degrading the pre-existing wave field. The subsequent power increases at these frequencies evident in *Figure 21*, c. days 39.0, 40.0, and 41.0 are due to the newly-evolving wind wave field.

The behavior of the microseism peak band is not as easily explained by the available data. The growth of power throughout days 38 and 39, as well as the shift towards lower frequencies apparent in *Figure 20(a)* suggests an evolving wind wave source. Similarly, the fall during day 40 and subsequent rise during day 41 suggests the demise of the old wave regime and domination of the new regime in response to winds which blew approximately 90°, then 180° with respect to the old wind.

If wind waves were soley responsible for the observed seismic noise variations, *Equation (4)* implies that a fall-off of the wind-wave spectrum would result in an ocean-bottom pressure spectrum $\propto f^{-7}$, rather than the observed f^{-5} (*Figure 13*). However, the ragged fall-off observed in all spectra suggests that the seafloor responded resonantly to the wind-wave forcing. Sharp peaks at approximately 0.35, 0.5, 0.65, and 0.8 Hz were observed in the borehole data. It will be recalled that the peaks at 0.5 and 0.65 Hz were prominent in one or more of the OBS spectra in *Figure 11*. Equal spacing of spectral peaks is expected for so-called 'organ pipe' modes, due to the reverberation of acoustic waves between the sea surface and the sediment-basement interface. Such reverberations are an important constituent of the seismic phase P_n observed in the ocean (Sereno and Orcutt[28]) which in this context is comprised of P waves travelling almost entirely in the upper mantle before turning sharply to the vertical in the sediment. The gravest peaks are at frequencies $(2n+1)\ df/2$, $n = 0, 1, ...$, and are therefore seperated by df, where df is the two-way travel time of a single reverberation. At the MSS site[28], df = 0.14, very near the observed 0.15 Hz. The nonlinear interaction of gravity waves described above doubtless generates acoustic waves in the compressible ocean (Longuet-Higgins[7], Hasselmann[8], Brekhovskikh[29], Hughes[30], Lloyd[31]), so that a significant contribution to the observed ambient noise, both acoustic and seismic, may be due to these reverberations. On the other hand, if the ocean-bottom pressure fluctuations due to the wind waves are spatially restricted, they must perforce possess energy over a broad range of wavenumbers, and therefore be capable of exciting trapped seismic modes which have a much smaller phase velocity than the "leaky" acoustic reverberations. Modelling the relative contributions to the ambient noise of these complementary wave types will be the topic of further research.

VI. CONCLUSIONS

The observations reported here constrain the source mechanisms and propagation modes of infrasonic and microseismic noise in the deep ocean. High coherences, 180° cross-phases, and ratios between displacement and pressure at frequencies below 1 Hz imply a trapped wave propagation mode. Modelling of these measurements, as well as the horizontal-component measurements, may further constrain the wave type, although a definitive experiment to measure the wavenumber spectrum may be required.

Episodic variations of the wind direction and speed correlate with changes in both acoustic and microseismic noise. In particular, a peak at 0.5 Hz responded immediately to sudden changes in wind direction, both in ocean-bottom and sub-bottom observations. The microseism peak is also affected by the wind, an observation that is in contrast to multitudes of previous reports focussing attention on swell as the chief agent of noise generation. The mechanism for transferring energy from wind to microseisms is presumably the non-linear interaction of wind-generated waves. Spectral shapes, and temporal evolution of pressure and displacement spectra support this hypothesis.

ACKNOWLEDGEMENTS

REFERENCES

1. H. Bradner, J. G. Dodds and R. E. Foulks, "Investigation of microseism sources with ocean-bottom seismometers, J. Geophys. Res. 69, 4339-4348 (1964).

2. Gary V. Latham and George H. Sutton, "Seismic measurements on the ocean floor, 1. Bermuda area," J. Geophys. Res.71 2545-2572 (1966).

3. Gary V. Latham, Rockne S. Anderson and Maurice Ewing, "Pressure variations produced at the ocean bottom by hurricanes," J. Geophys. Res. 72, 5693-5704 (1967).

4. R. H. Nichols, "Infrasonic ambient ocean noise measurements: Eleuthera," J. Acoust. Soc. Am. 69, 974-981 (1981).

5. Charles Cox, Thomas Deaton and Spahr Webb, "A deep-sea differential pressure gauge," J. Atmosph. Oceanic Tech., 1, 237-246 (1984).

6. Gary V. Latham and Ali A. Nowroozi, "Waves, weather, and ocean bottom microseisms," J. Geophys. Res. 73:3945-3956 (1968).

7. M. S. Longuet-Higgins, "A theory of the origin of microseisms," Phil. Trans. Roy. Soc., A. 243, 1-35 (1950).

8. K. Hasselmann, "A statistical analysis of the generation of microseisms," Rev. Geophys. 1 177-210 (1963).

9. R. A. Haubrich, W. H. Munk and F. E. Snodgrass, "Comparative spectra of microseisms and swell," Bull. Seism. Soc. Amer.53 27-37 (1963).

10. Alick C. Kibblewhite and Kevin C. Ewans, "Wave-wave interactions, microseisms, and infrasonic ambient noise in the ocean," University of Texas at Austin Applied Research Laboratories Report ARL-TR-84-2 (1984).

11. Willard J. Pierson, Jr., and Lionel Moskowitz, "A proposed spectral form for fully developed wind seas based on the similarity theory of S. A. Kitaigorodskii," J. Geophys. Res. 69, 5181-5190 (1964).

12. K. Hasselmann, T. P. Barnett, E. Bouws, H. Carlson, D. E. Cartwright, K. Enke, J. A. Weing, H. Gienapp, D. E. Hasselmann, P. Kruseman, A. Meerburg, P. Müller, D. J. Olbers, K. Richter, W. Sell and H. Walden, "Measurement of wind-wave growth and swell decay during the Joint North Sea Wave Project (JONSWAP)," Ergänzungsheft zur Deutschen Hydrographischen Zeitschrift Reine A(8 °) (12), 122 pp (1973).

13. Kimmo K. Kahma, "A study of the growth of the wave spectrum with fetch," Journ. Phys. Ocean. 11, 1503-1515 (1981).

14. J. A. Ballard, C. C. Mulcahy, R. C. Wallerstedt and E. L. Kiser, "The borehole seismic experiment in Hole 395A: Engineering and installation," in *Initial Reports of the Deep Sea Drilling Project*, edited by R. D. Hyndman, M. H. Salisbury, et al.(U. S. Government Printing Office, Washington, 1984), Vol. 78, pp. 743-758.

15. Gordon G. Sorrells, "A preliminary investigation into the relatio.iship between long-period seismic noise and local fluctuations in the atmospheric pressure field," Geophys. J. R. Astr. Soc. 26, 71-82 (1971).

16. R. D. Moore, L. Dorman, C.-Y. Huang and D. L. Berliner, "An ocean bottom, microprocessor based seismometer," Mar. Geophys. Researches 4, 451-477 (1981).

17. John A. Orcutt, Robert D. Moore and Thomas H. Jordan, "Description and performance of the Scripps ocean bottom seismographs during the Ngendei Experiment," submitted to: The Initial Reports of the Deep Sea Drilling Project, Volume 88/91 (1985).

18. K. C. Creager and L. M. Dorman, "Locations of instruments on the seafloor by joint adjustment of instrument and ship positions," J. Geophys. Res. 87, 8379-8388 (1982).

19. P. D. Welch, "The use of fast Fourier transform for the estimation of power spectra: A method based on time averaging over short, modified periodograms," IEEE Trans. Audio Electro-acoust. AU-15, 70-73 (1967).

20. G. C. Carter, C. H. Knapp, and A. H. Nuttall, "Estimation of the magnitude-squared coherence function via overlapped fast Fourier transform processing," IEEE Trans. Audio Electroacoust. AU-21, 337-344 (1973).

21. J. S. Bendat and G. G. Piersol, *Random data: Analysis and measurement procedures*, (John Wiley, New York, 1971).

22. R. A. Fischer, "The general sampling distibution of the multiple correlation coefficient," Proc. Roy. Soc.,Ser. A 121 654-673 (1928).

23. R. J. Urick, *Principals of Underwater Sound* (McGraw-Hill, New York, 1983), 3rd edition.

24. Hugh Bradner, "Pressure variations accompanying a plane wave propagated along the ocean bottom," J. Geophys. Res. 68, 3465-3471 (1963).

25. W. A. Schneider and M. M. Backus, "Ocean-bottom seismic measurements off the California coast, "J. Geophys. Res. 69, 1135-1143 (1964).

26. Spahr Chapman Webb, *Observations of Seafloor Pressure and Electric Field Fluctuations,* Ph.D. thesis, University of California (1984).

27. G. L. Tyler, C. C. Teague, R. H. Stewart, A. M. Peterson, W. H. Munk and J. W. Joy, "Wave directional spectra from synthetic aperture observations of radio scatter," Deep-Sea Res. 21, 989-1016 (1977).

28. Thomas Sereno and John Orcutt, "The synthesis of realistic oceanic P_n wavetrains," J. Geophys. Res., *in press* (1985).

29. L. M. Brekhovskikh, "Underwater sound generated by surface waves in the ocean," Izv. Atmospheric and Oceanic Physics 2, 970-980 (1966).

30. B. Hughes, "Estimates of underwater sound (and infrasound) produced by nonlinearly interacting ocean waves," J. Acoust. Soc. Am. 60, 1032-1039 (1976).

31. Stuart P. Lloyd, "Underwater sound from surface waves according to the Lighthill-Ribner theory," J. Acoust. Soc. Am. 69, 425-435 (1981).

FIGURE CAPTIONS

Figure 1   Displacement responses of (a) ocean-bottom seismograph (OBS) and (b) Marine Seismic System (MSS) instrumentation used during the Ngendei experiment. (a) OBS seismometer and hydrophone responses. Two responses were available for the OBS's (ocean bottom seismographs). (b) The Gould MSS mid-period (MP) and short-period (SP) responses differ from the Teledyne responses by the low-pass FIR (Finite Impulse Response) digital filter shown with dashed lines.

Figure 2   Locations of the MSS and six OBS's during the refraction experiment. See text for explanation of symbols. (a) Configuration of the four capsules which recorded refraction signals (Juan, Karen, Lynn, and Suzy). (b) Configuration of the two OBS's which concurrently recorded teleseismic signals in a triggered mode (Janice and Phred).

Figure 3   (a) and (b): Locations of the OBS's during the teleseismic experiment. See text for explanation of symbols.

Figure 4   Spectral power density estimates of typical MSS noise samples compared to system noise levels. The spectra, given in $counts^2/Hz$, have not been corrected for instrument response. (a) Gould Channel MZ. (b) Gould channel SB. (c) Teledyne channel SB.

Figure 5   Coherence spectra, corrected for alignment, between (a) Teledyne and Gould channel MZ, (b) Teledyne and Gould channel SB, and (c) Teledyne channels SZ and SB.

Figure 6   Comparison of noise spectrum obtained with the teleseismic (solid upper curve) and refraction (dashed upper curve) OBS responses. The corresponding instrument-corrected sampling noise spectra (lower curves) are also shown.

Figure 7 Demonstration of *Melville's* ship noise during the period 034:0430-035:0000 (Julian date). (a) Smoothed, integrated OBS Suzy vertical component power density between 17.9 and 18.2 Hz. (b)*Melville's* range from the MSS site.

Figure 8 Illustration of ship noise in the (a) OBS and (b) MSS data. Solid spectra were observed when ships were nearby and operational, and the dashed spectra when ships were completely absent (OBS) or still nearby (MSS). MSS data are not available at any time when ships were completely absent.

Figure 9 Simultaneous vertical-component displacement power densities at the ocean bottom (dashed line) and in the borehole (solid line).

Figure 10 Simultaneous horizontal-component displacement power densities at the ocean bottom (dashed line) and in the borehole (solid line).

Figure 11 A comparison of simultaneous vertical (solid) and horizontal (dashed) power densities in the borehole.

Figure 12 A comparison of simultaneous vertical (solid) and horizontal (dashed) power densities at the ocean-bottom.

Figure 13 Ocean-bottom pressure measurements concurrent with the displacement spectra of Figures 9-12.

Figure 14 (a) Coherence and (b) cross-phase between OBS Suzy channels Z (vertical) and P (hydrophone). The cross-phase, plotted in multiples of π, has been corrected for instrument response phase. (c) The ratio between OBS Suzy pressure and vertical ground velocity power densities, normalized by the product of density and acoustic speed in the water.

Figure 15 (a) Coherence and (b) cross-phase between the vertical channels of OBS's Suzy and Lynn, as for Figure 14.

Figure 16 (a) Coherence and (b) cross-phase between the hydrophone channels of OBS's Suzy and Lynn, as for Figure 14.

Figure 17 *Challenger* decklog observations of (a) wind and (b) swell depicted as vectors with origin at the time of measurement, lengths proportional to wind speed (knots) or swell height (feet), and direction that of the measurement. The swell measurements are plotted at a level corresponding to swell period.

Figure 18 Variation with time of OBS Phred vertical-component acceleration power in the frequency band 0.1 - 1.0 Hz.

Figure 19 Temporal variation of (b) peaks at 0.2 and 0.5 Hz of the OBS Phred data shown in Figure 18 compared with (a) wind and (c) swell observations shown in Figure 17.

Figure 20 Temporal variation of vertical accleration in the borehole in the frequency bands (a) 0.1 - 1.0 Hz and (b) 0.4 - 0.9 Hz.

Figure 21 Temporal variation of (b) peaks at 0.2 and 0.5 Hz of the MSS data shown in Figure 20 compared with (a) wind and (c) swell observations shown in Figure 17.
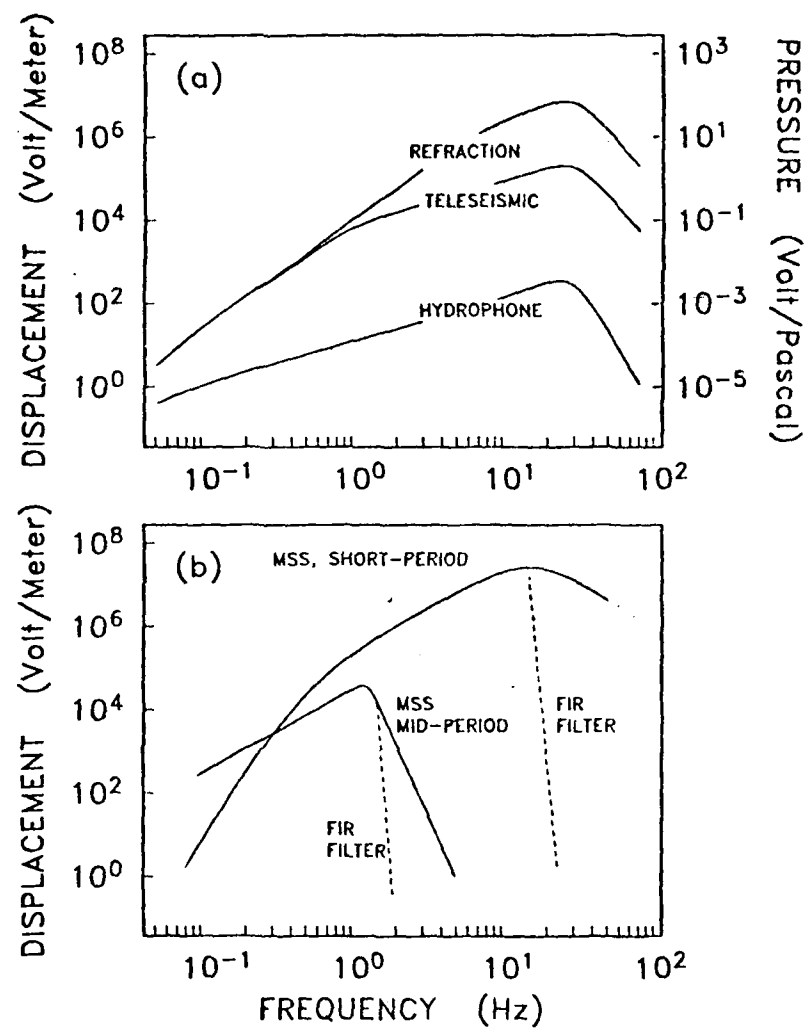
Figure 1.

OBS Locations

Refraction Experiment
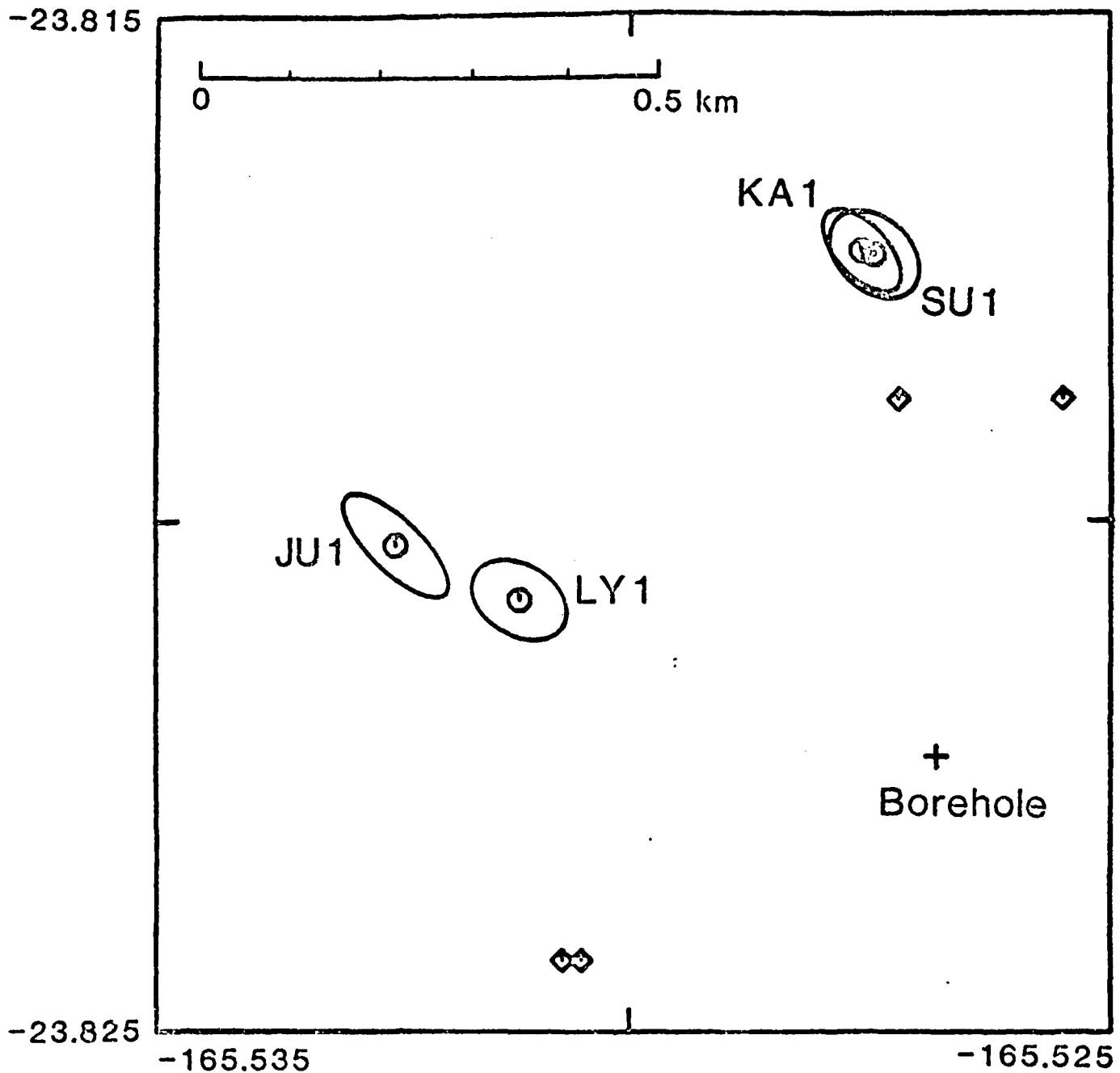
FIGURE 2 (a)

OBS Locations

Initial Teleseismic Experiment
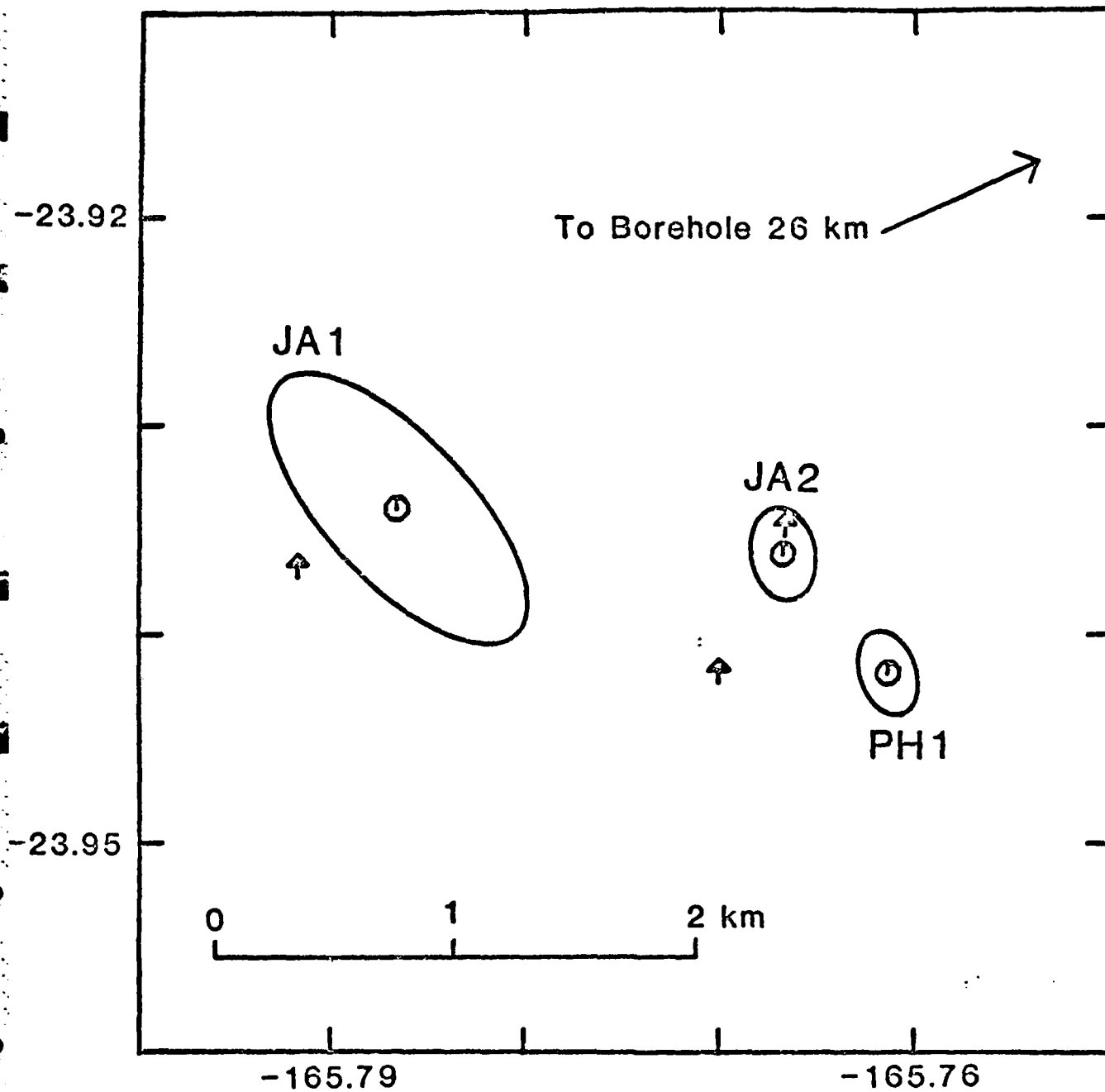
FIGURE 2 (b)

OBS Locations

Teleseismic Experiment

FIGURE 3 (a)

FIGURE 3 (b)

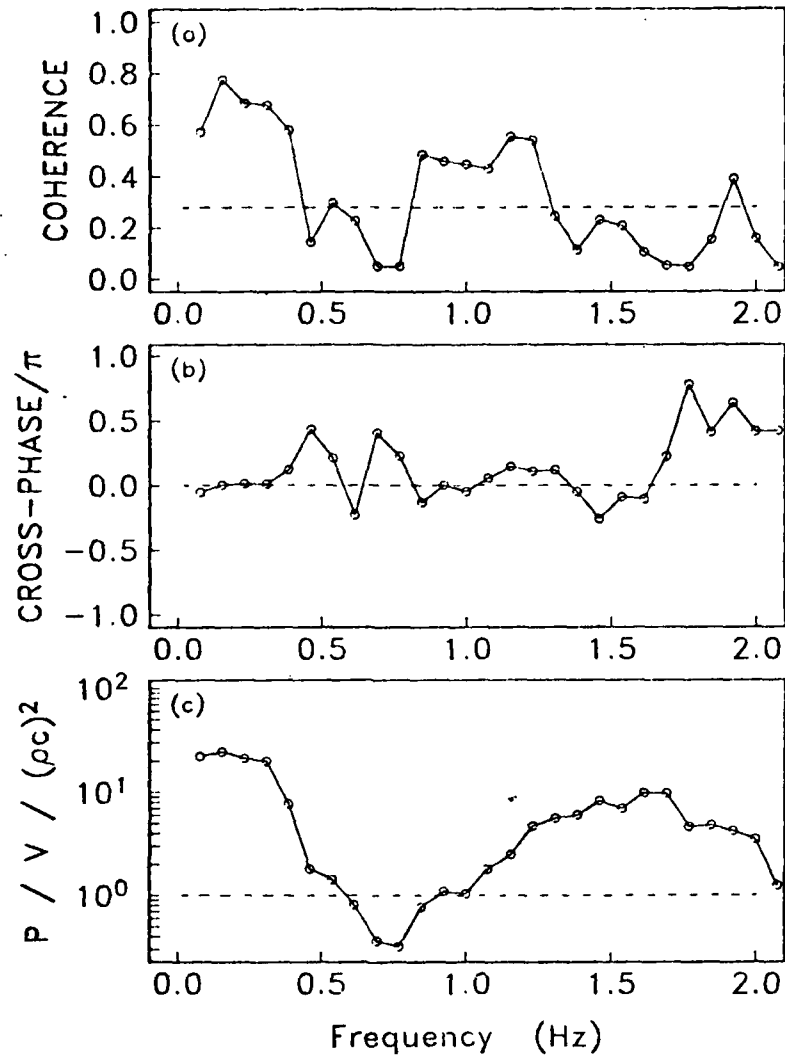OBS Locations

Teleseismic Experiment
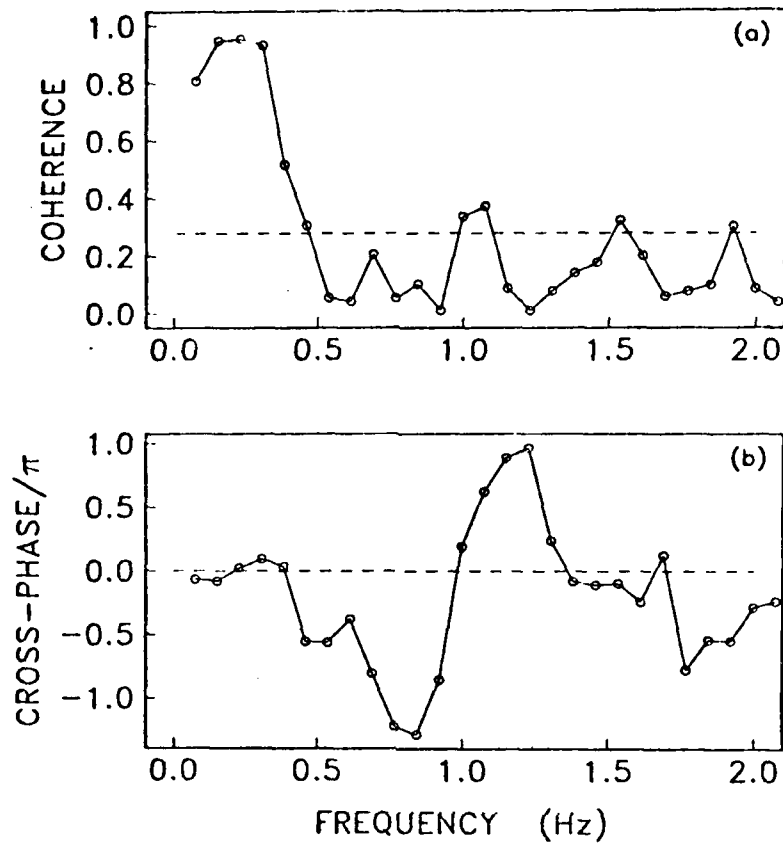
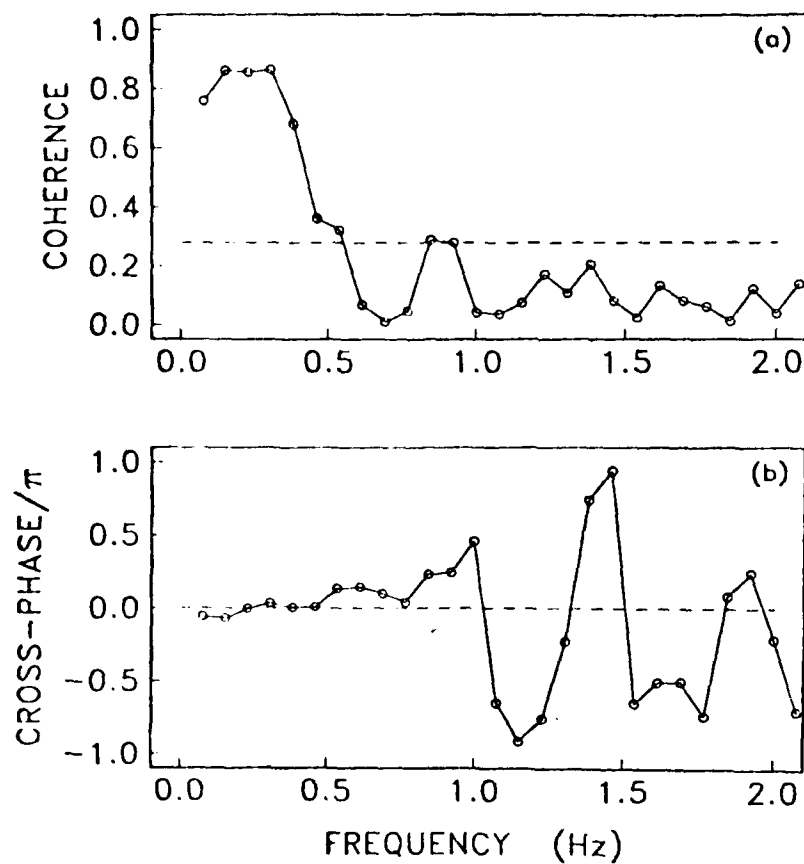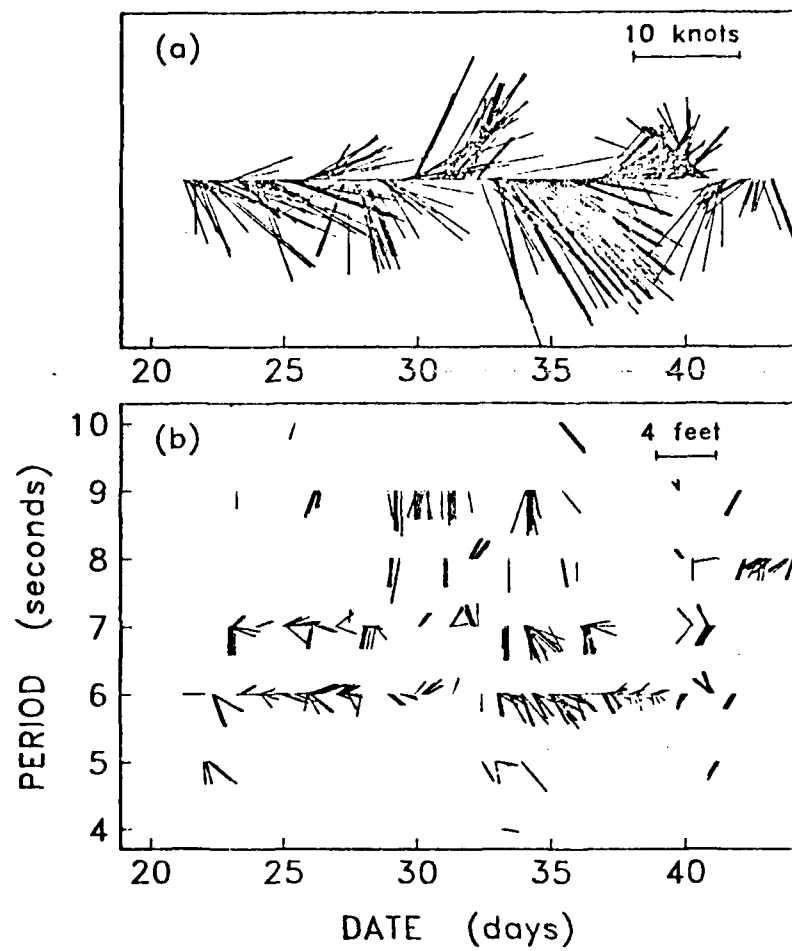JA3

+ Borehole

KA2

PH3

LY2

1 km

0

-165.53

-165.55

-23.81

-23.82
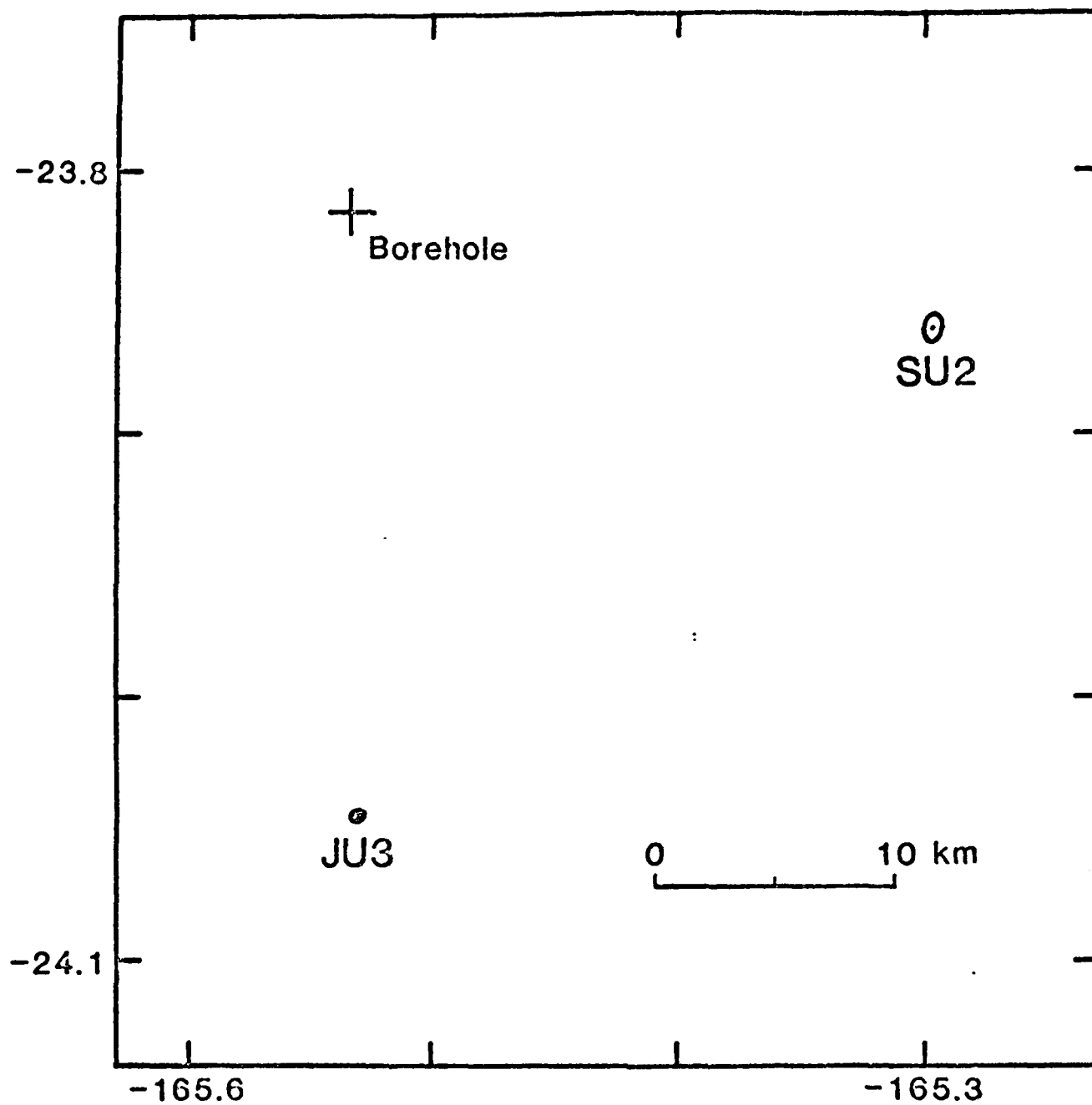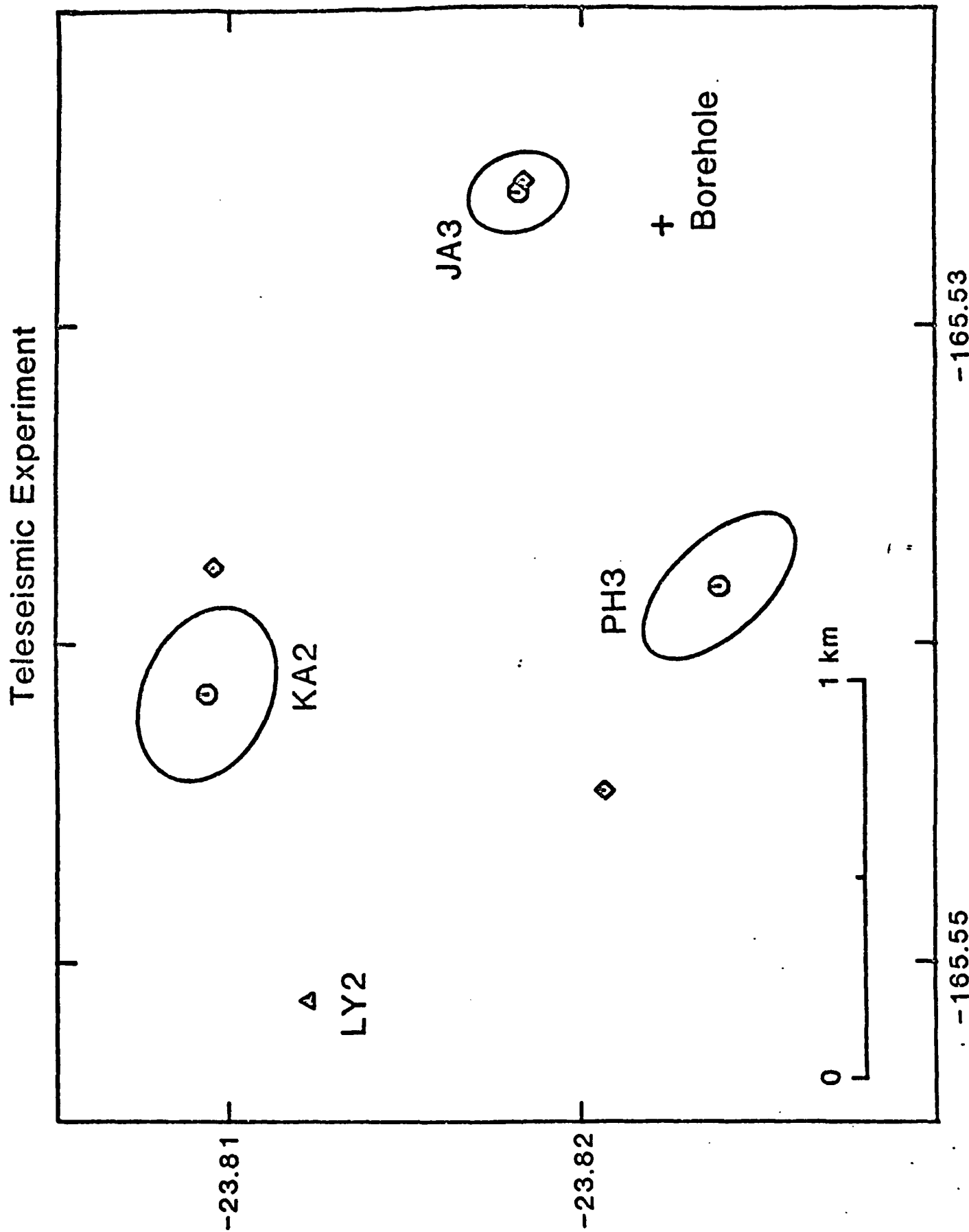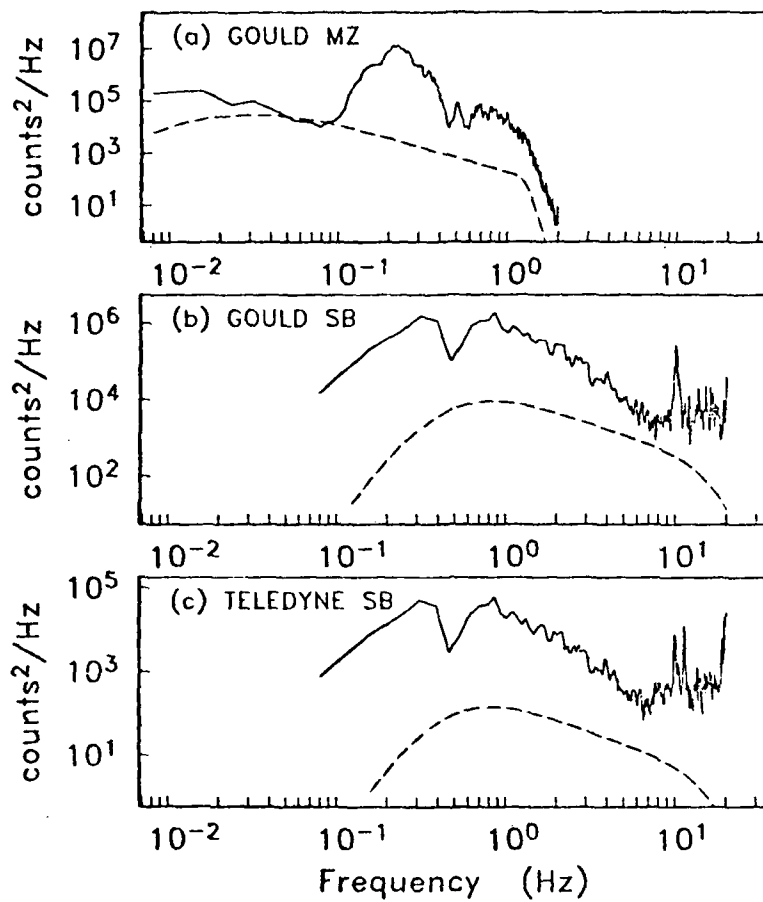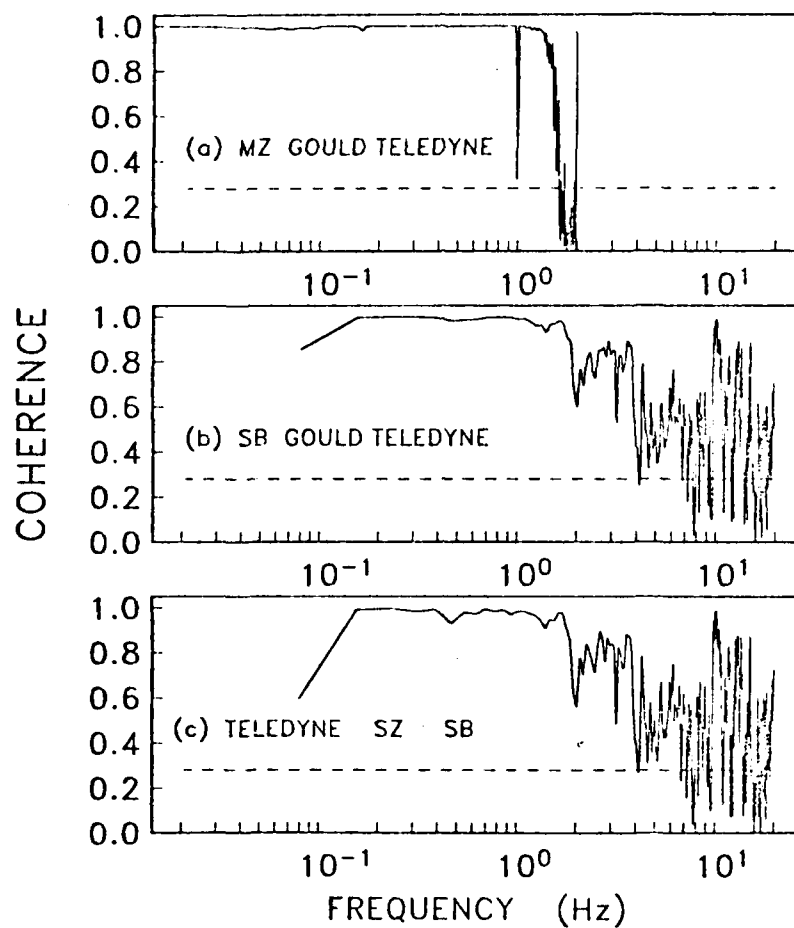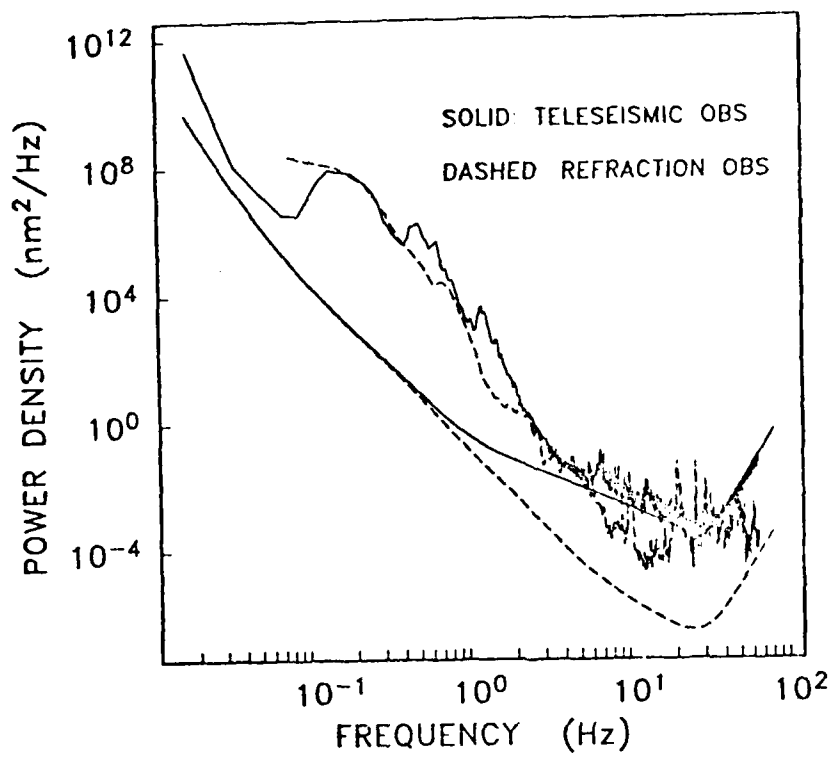
Figure 4.

Figure 5.

Figure 6.
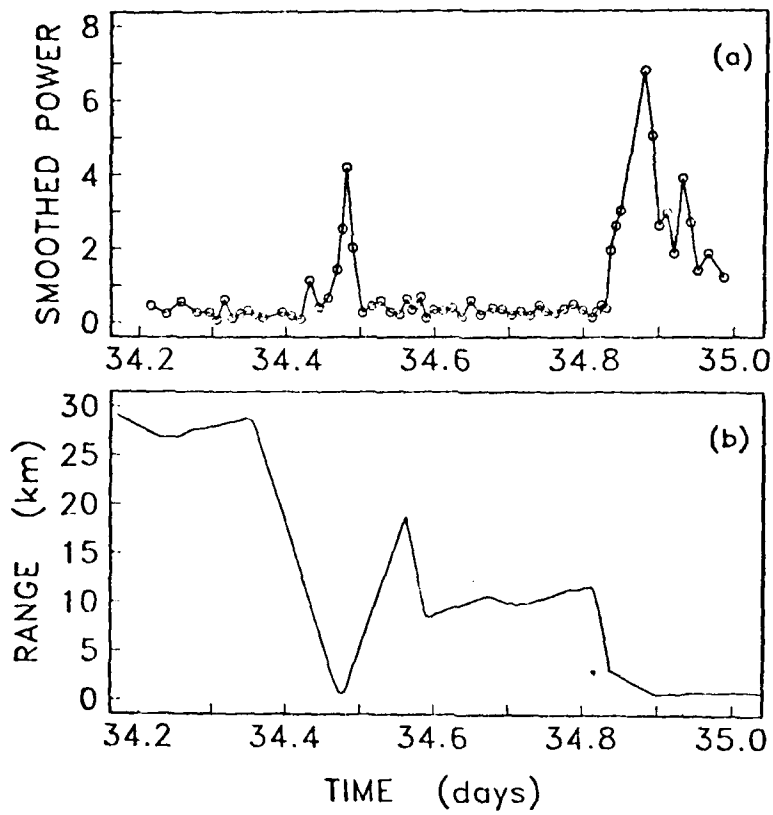
Figure 7.
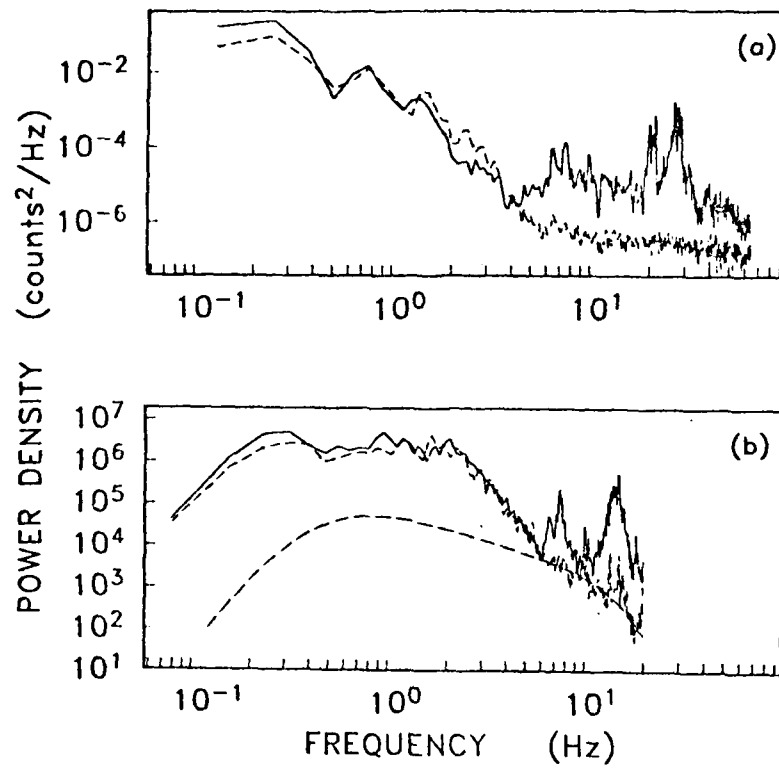
Figure 8.
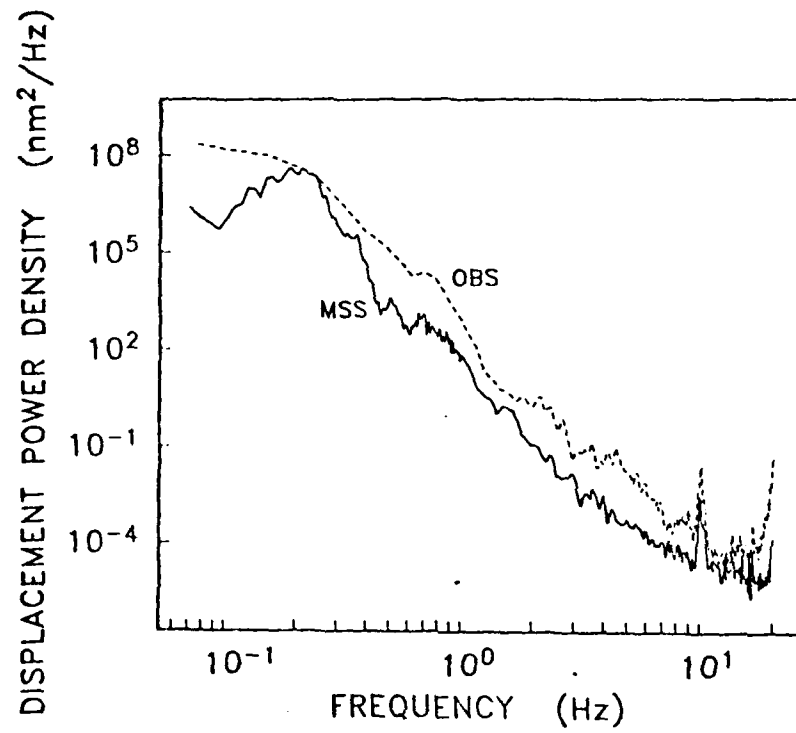
Figure 9.
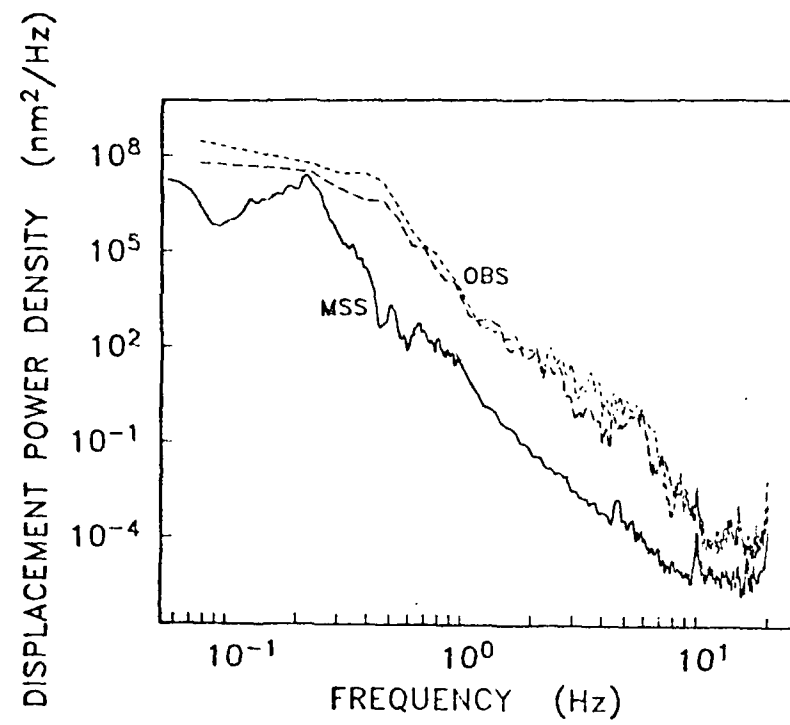
Figure 10.
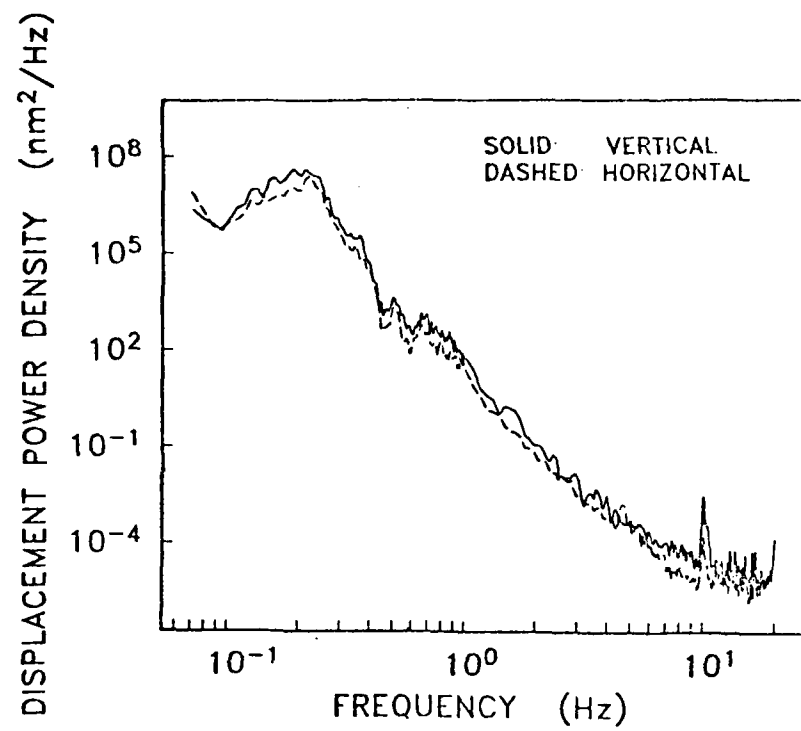
Figure 11.
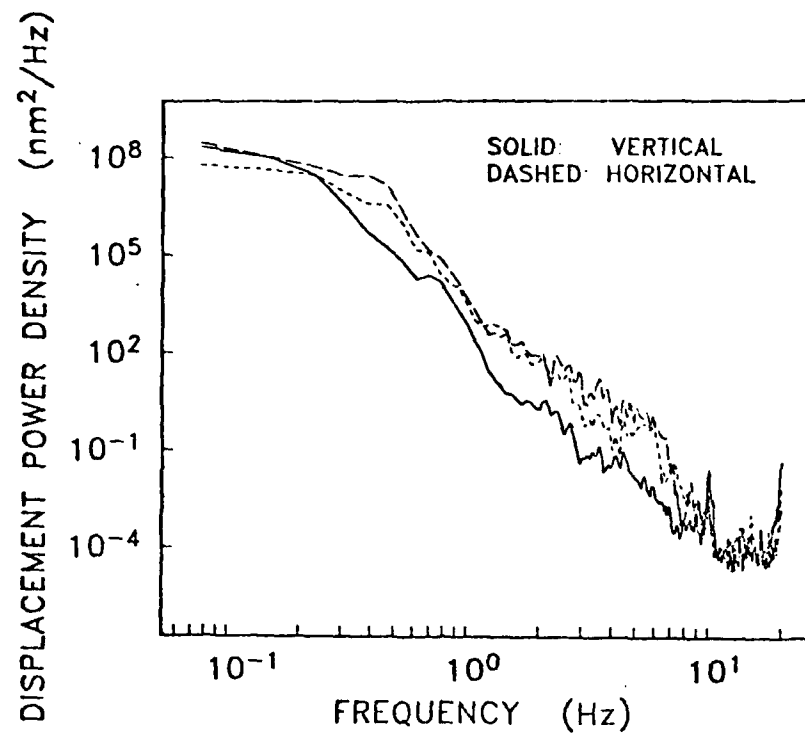
Figure 12.
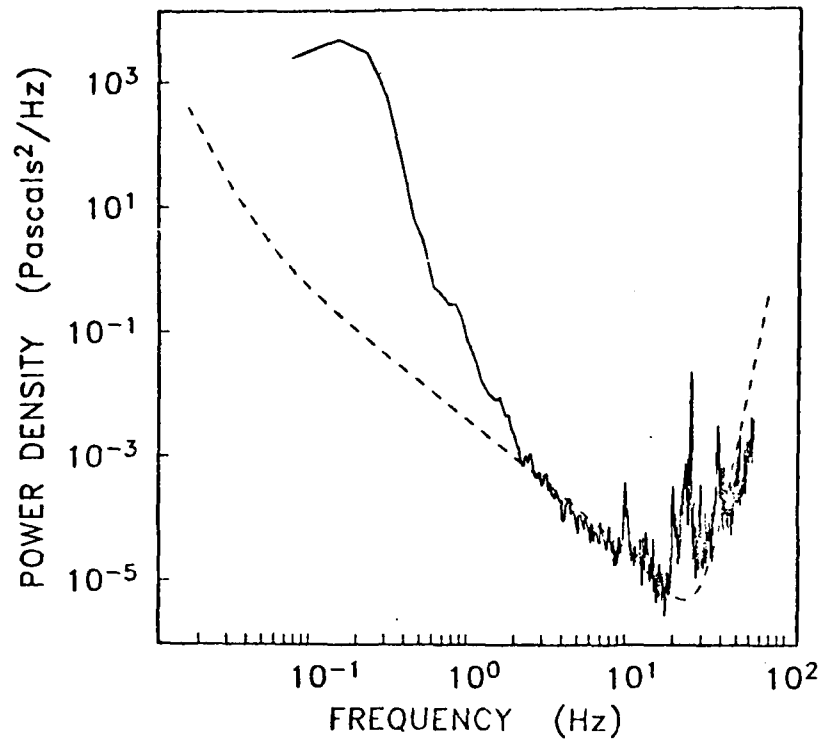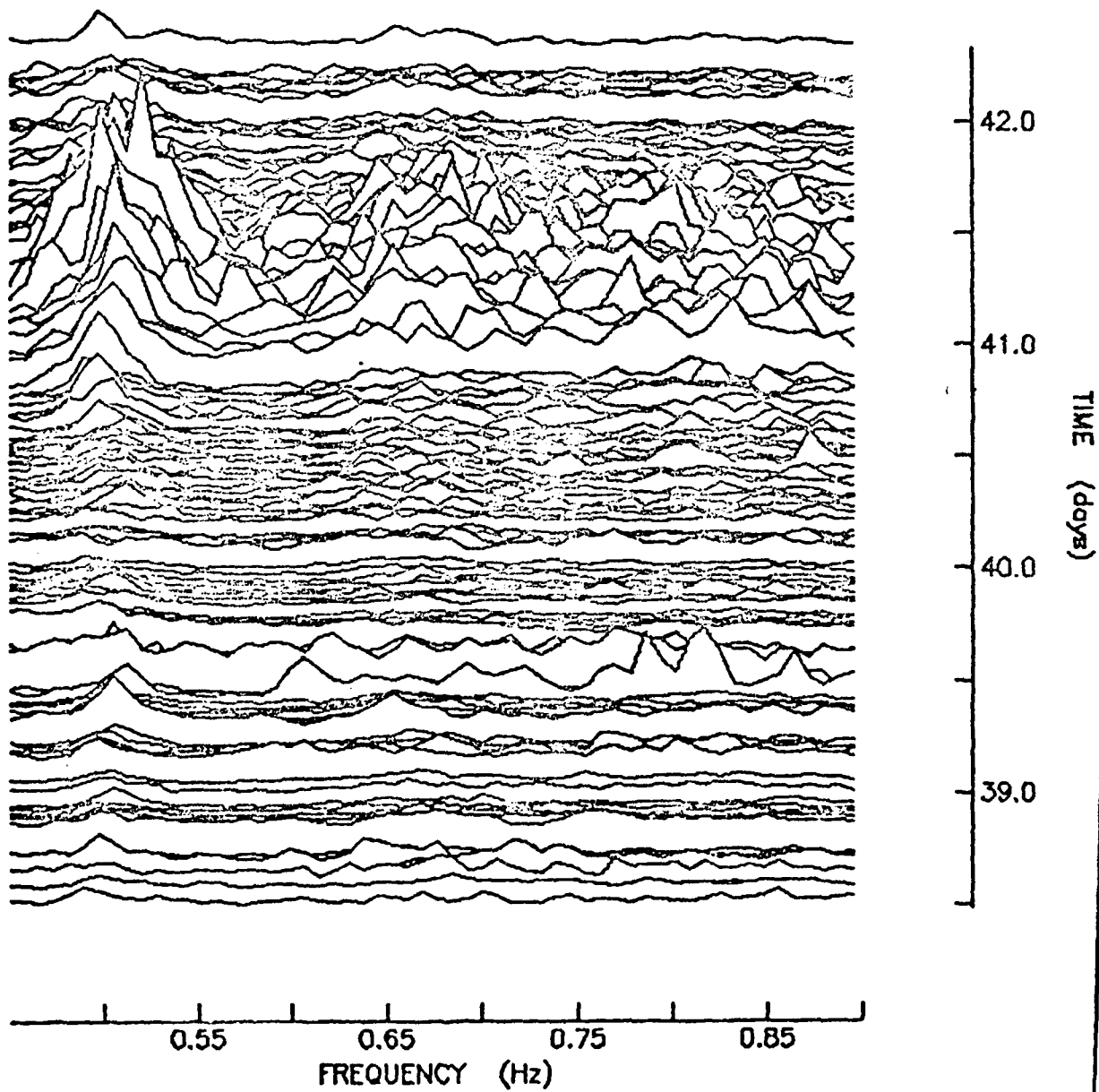
Figure 13.

Figure 14.

Figure 15.

Figure 16.

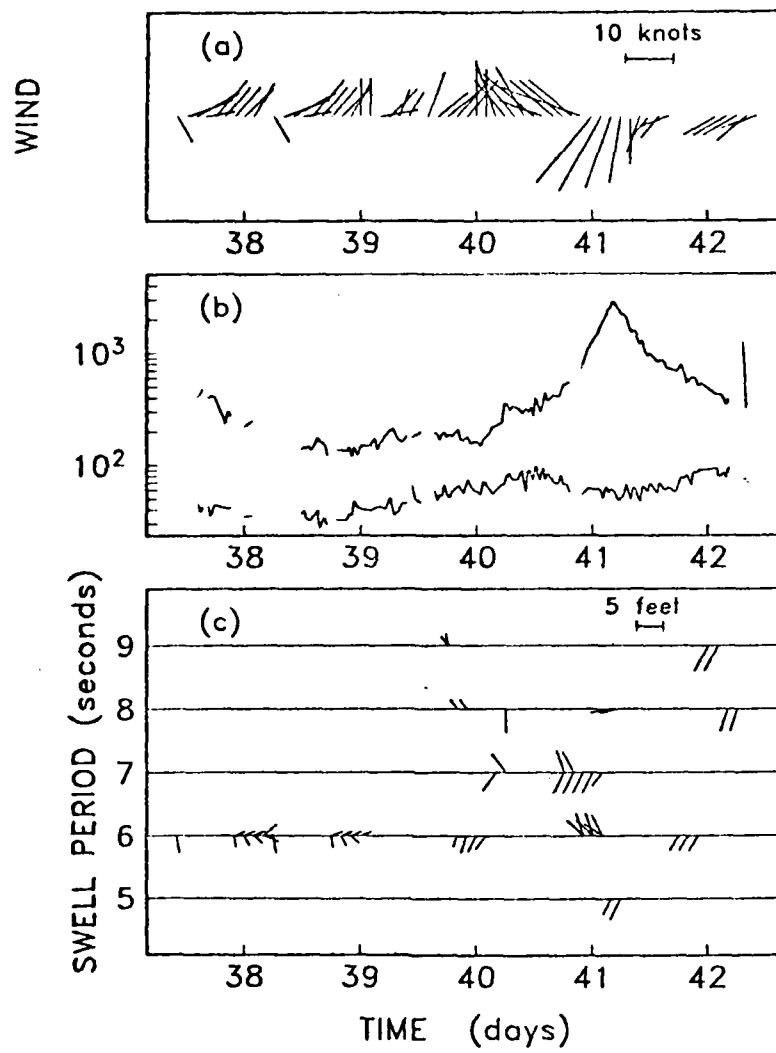Figure 17.

FIGURE 18
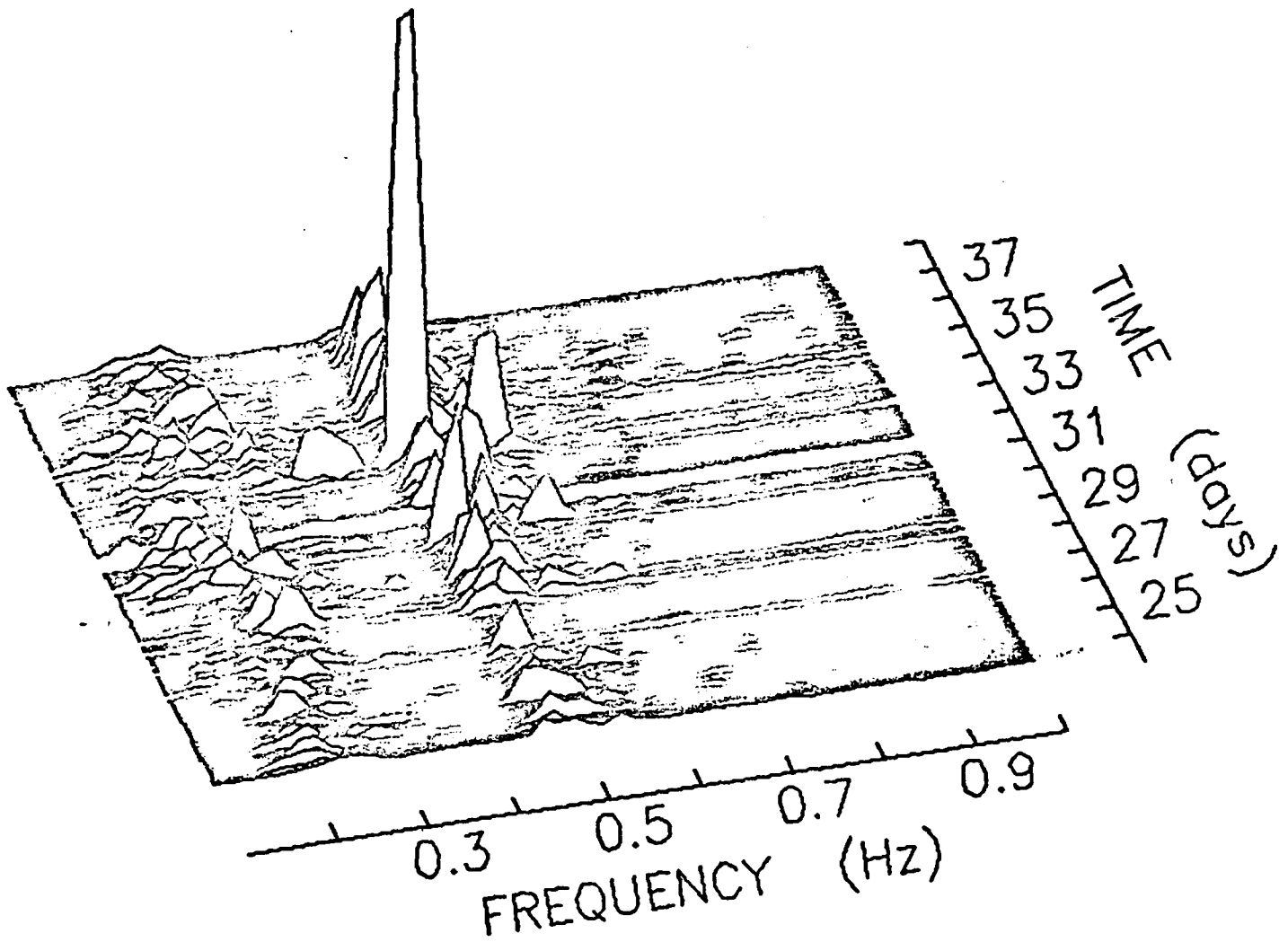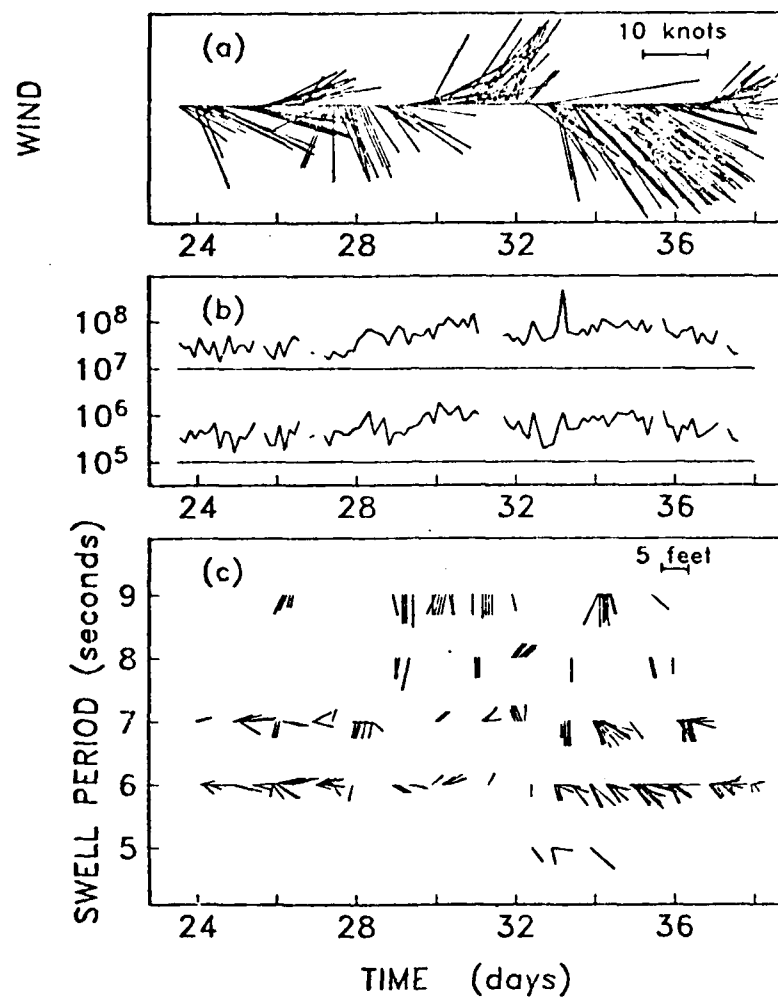
Figure 19.
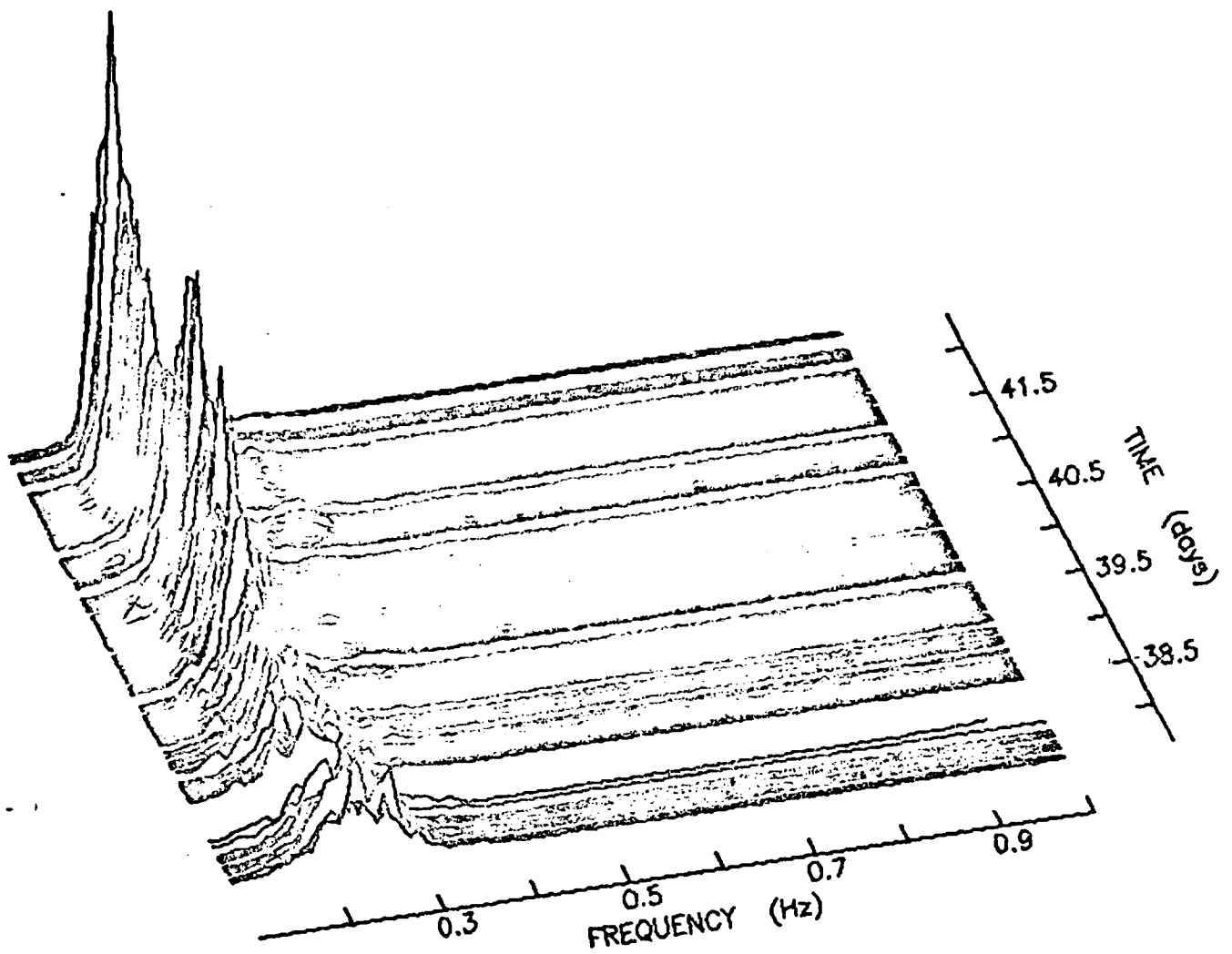
FIGURE 20 (a)

FIGURE 20 (b)

Figure 21.